COMPUTATIONAL FLUID DYNAMICS SIMULATION OF THREE-DIMENSIONAL PARALLEL JETS

A Dissertation
Presented to
The Academic Faculty

by

Zhihang Liu

In Partial Fulfillment
of the Requirements for the Degree
Master of Science in the
Computational Science & Engineering

Georgia Institute of Technology
December 2018

COMPUTATIONAL FLUID DYNAMICS SIMULATION OF THREE-DIMENSIONAL PARALLEL JETS

Approved by:

Dr. Lakshmi Sankar Advisor
School of Aerospace Engineering
Georgia Institute of Technology

Dr. Jechiel Jagoda
School of Aerospace Engineering
Georgia Institute of Technology

Dr. Edmond Chow
School of Computational Science & Engineering
Georgia Institute of Technology

Date Approved: [November 30, 2018]

ACKNOWLEDGEMENTS

I would first like to thank my thesis advisor Dr. Sankar. The door to Prof. Sankar's office was always open whenever I ran into a trouble spot or had a question about my research or writing. He consistently allowed this paper to be my work but steered me in the right the direction whenever he thought I needed it.

I would also like to thank Dr. Jagoda and Dr. Chow for serving as committee members of my thesis proposal and defense. Their suggestions and guidance were very helpful in completing this study.

I would also like to acknowledge Dr. Haynes at the Kimberly Clark Corp. I am thankful to him for providing all the input and sharing his encyclopedic knowledge of this topic. His industry experience and the real-world data was invaluable.

Finally, I would also like to thank my wife and my family. Without their support and love, I do not know whether I could have finished this work by myself.

TABLE OF CONTENTS

LIST OF TABLES

LIST OF FIGURES

LIST OF SYMBOLS AND ABBREVIATIONS

k	Turbulence kinetic energy
ω	Specific dissipation rate
u_i	Instantaneous velocity
$\overline{u_i}$	Time average velocity
u_i'	Fluctuating velocity
x_i	Cartesian vector
t	Time
p	Static pressure
δ_{ij}	Kronecker delta
ϵ	Turbulent dissipation rate
μ	Dynamic viscosity
τ_{ij}	Shear stress tensor
T	Total pressure
P	Gauge pressure (psi)
μ_t	Turbulent viscosity
α	Permeability of the porous media

SUMMARY

High-speed air jets are often used in industries for manufacturing thin fibers through a process known as melt-blowing (MB). For a high quantity of fibers to be produced, many small-scale jets placed side by side are used. These jets draw the air from the same compressed air storage tank. Therefore, the fiber formation is critically dependent on the aerodynamics of the jet flow field. Real word MB devices always have complicated internal structures such as mixing chambers and air channels between the air tank and the jet exit, which may trigger flow instabilities and generate a turbulent cross flow at the jet exit. The turbulent unsteady flow would have a significant impact on the formation of fibers and nonwoven webs. The purpose of this study is to understand the effect of the internal geometry on the jet flow field and explore passive concepts for prevention of flow instabilities within the flow passages.

This study consists of three parts. A baseline case without any passive fluctuation reduction devices was studied to understand the mechanism of the instability and to investigate the details of the internal flow field. Next, a wire mesh screen was placed between the air plates and the die tip, to study its effect on both the velocity and pressure distribution across the screen. Finally, a honeycomb structure was installed near the exit of last mixing chamber. The effectiveness of these two flow fluctuation reduction devices was compared in detail using time series measurements and time-dependent flow field contours.

CHAPTER 1. INTRODUCTION

1.1 Research Background

High-speed air jets are often used in industry for manufacturing thin fibers through a process known as melt-blowing (MB) (Shambaugh, 1988; Zuo et al., 2013). In melt blowing, High-velocity gas streams impinge upon molten strands of polymer to produce fine filaments (see Figure 1). A sketch of an MB system used by industry is shown in Figure 2. In this approach, two jets are placed at an angle of approximately 60 degrees to each other. Please see US Patent 6,972,104 B2 by Haynes et al (Haynes, B. D & Cook, 2005). for the details of an innovative production process.

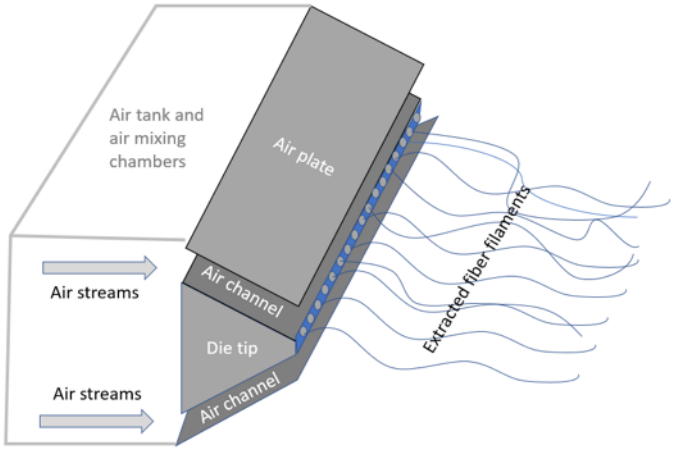

Figure 1 - 3D model of the Melt-blowing system

Fiber formation during the MB process is critically dependent on the aerodynamics of the process. The 2-D rectangular air jets are inherently unstable because of the inflection point that occurs in the shear layer (a layer of sharp velocity gradient). Small disturbances, either fluid dynamic or acoustic in nature, can amplify in space and time. The amplified flow

fluctuations would cause the shear layers to oscillate in space and time and eventually become turbulent. When two impinging jets are placed near each other, new modes of instability may arise, causing the flow downstream of the impingement to oscillate (or flap) laterally. These oscillations would adversely affect the fiber generation process.

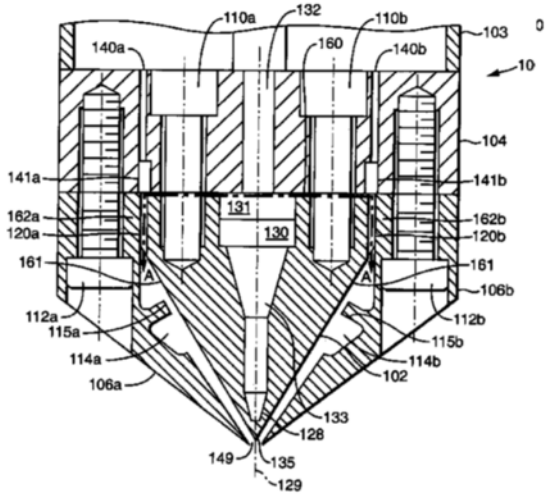

Figure 2 - Sketch of a melt blowing system

1.2 Literature Review

In recent years, computational fluid dynamic (CFD) technology has been being used to study the airflow field of various melt-blowing dies. Melt blowing devices, especially the nozzle regions, have been studied experimentally (Krutka, Shambaugh, & Papavassiliou, 2002; Obot, Trabold, Gandhi, & Graska, 1986). In these experiments, the velocity of the flow field at several locations downstream of the die tip was measured using a cylindrical Pitot-tube. However, the cylindrical pitot-tube could only measure a single component of the three-dimensional velocity field. Other techniques, such as laser Doppler velocimetry (LDV) and hot wire anemometry, can provide one, two, or three components

of the velocity field. Because of the complexity of industry production environment, it is difficult to obtain velocity data, pressure data, and temperature data very close to the die tip with the above techniques.

The use of well validated CFD tools can avoid such limitations and save the cost of building the dies and running experimental tests. Holly et al. and Wang studied the effect of the turbulence model (Krutka et al., 2002; Wang & Wang, 2014), and the effect of shapes of die tip (Krutka et al., 2002). Hassan et al. investigated the effect of different air constrictors below the die tip. Sum et al. studied the MB process with different die width, slot angle, head width, and setback and compared the results of 2D and 3D simulations (Sun, Liu, Wang, & Zeng, 2011). The melt blowing process is a three-dimensional unsteady flow, and these past studies were primarily for 2-D jets, with an assumption that the flow is homogeneous in the longitudinal direction of the blowing die (the direction perpendicular to the paper in 2).

1.3 Research Objectives

The objective of this work is to understand the instability mechanisms of 3D jets interacting with each other and explore ways of suppressing these instabilities. The fibers that are present in the flow will not be modeled in these initial studies because they are several orders of magnitude thinner than the jet thickness, and do not significantly alter the flow. We start with a CAD model of the whole melt blowing system including air channels, mixing chamber, die body, die tip, and the two air plates. Only a small slice segment of the whole system was modeled, and the interfaces were modeled using a spanwise periodic boundary condition. This study consists of three parts. A baseline case was first studied

and included grid and time step studies and choice of a suitable turbulence model. Convergence of the flow field to a limit cycle behavior was also examined. Next, two passive fluctuation reduction devices- a wire mesh screen, and a honeycomb - were computationally modeled. Finally, flow visualization studies and time series analyses were done to understand the effectiveness of these passive devices in suppressing flow oscillations.

CHAPTER 2. NUMERICAL PROCEDURES

A commercial CFD solver, ANSYS FLUENT 18.0, was used to do all the simulations. The ANSYS FLUENT has been proved to be reliable on different fluid simulation problems, especially for the complex internal and external flow geometries. This solver includes structured and unstructured grid generation capabilities and flow visualization capabilities. Important parameters such as Turbulence Kinetic Energy, path lines and velocity field can be readily visualized and compared with different setups.

2.1 Turbulence Modelling

ANSYS FLUENT provides multiple choices of turbulence model ranging from one equation Spalart-Allmaras model to the most elaborate six equation Reynold-stress model. The turbulent flow calculations are all based on the Reynolds (ensemble) Averaging (Tennekes & Lumley, 1972). In Reynolds averaging, the solution variables in the instantaneous (exact) Navier-Stokes equations are decomposed into the mean (ensemble-averaged or time-averaged) and fluctuating components. For the velocity components:

$$u_i = \overline{u_i} + u_i' \tag{1}$$

Where $\overline{u_i}$ and u_i' are the mean and fluctuating velocity components.

For other scalar quantities similarly, we have $\phi = \bar{\phi} + \phi'$.

Substituting Equation (1) into the instantaneous continuity and momentum equations and taking the time average yields the ensemble-averaged momentum equations. The resulting forms may be written in Cartesian tensor form as:

$$\frac{\partial \rho}{\partial t} + \frac{\partial}{\partial x_i}(\rho u_i) = 0 \tag{2}$$

$$\frac{\partial}{\partial t}(\rho u_i) + \frac{\partial}{\partial x_j}(\rho u_i u_j) = -\frac{\partial p}{\partial x_i} + \frac{\partial}{\partial x_j}\left[\mu\left(\frac{\partial u_i}{\partial x_j} + \frac{\partial u_j}{\partial x_i} - \frac{2}{3}\delta_{ij}\frac{\partial u_k}{\partial x_k}\right)\right] + \frac{\partial}{\partial x_j}(-\rho\overline{u_i' u_j'}) \tag{3}$$

Equation (2) and Equation (3) are collectively called Reynolds-averaged Navier-Stokes (RANS) equations. They have the same general form as the instantaneous Navier-Stokes equations, with the velocities and other solution variables now representing ensemble-averaged (or time-averaged) values. Additional terms now appear that represent the effects of turbulence. This Reynolds stresses term $-\rho\overline{u_i' u_j'}$ must be modeled before the RANS Equations can be computationally solved.

There are two approaches to modeling the Reynolds stress term: Boussinesq approach and Reynolds Stress Transport Models. In most cases, models based on the Boussinesq hypothesis perform very well, and the additional computational expense of the Reynolds stress model is not justified. A common method employs the Boussinesq hypothesis to relate the Reynolds stresses to the mean velocity gradients as shown below:

$$-\rho\overline{u_i'u_j'} = \mu_t\left(\frac{\partial u_i}{\partial x_j}+\frac{\partial u_j}{\partial x_i}\right)-\frac{2}{3}\left(\rho k+\frac{\mu_t\partial u_k}{\partial x_k}\right)\delta_{ij} \quad (4)$$

The quantity μ_t may be computed using a variety of turbulence models such as the Spalart-Allmaras model, $k-\omega$ model, and the $k-\epsilon$ turbulence model. The advantage of this approach is the low computational cost associated with the computation of the turbulent viscosity compared to the direct resolution of the large eddies. Only one or two additional equations are solved depending on the turbulence model. For instance, in the case of $k-\omega$ model, the turbulence kinetic energy k and the specific dissipation rate ω are solved. The disadvantage of the Boussinesq hypothesis as presented is that it assumes μ_t is an isotropic scalar quantity, which is not always true for all turbulent flows. However, the assumption of an isotropic turbulence viscosity typically works well for shear flows dominated by only one of the turbulent shear stresses. This covers the flow in this research where we focus on the wall boundary in the air channel and the mixing layer and jets in the flow field outside the die.

The standard $k-\omega$ model was used to model the turbulent flow. The difference of $k-\omega$ models and $k-\epsilon$ models has been discussed in (Krutka et al., 2002). The Standard $k-\omega$ model in ANSYS FLUENT is based on the Wilcox $k-\omega$ model. The turbulence kinetic energy k, and the specific dissipation rate, ω, are obtained from the following transport equations:

$$\frac{\partial}{\partial t}(\rho k) + \frac{\partial}{\partial x_i}(\rho k u_i) = \frac{\partial}{\partial x_j}\left(\Gamma_k \frac{\partial k}{\partial x_j}\right) + G_k - Y_k \quad (5)$$

$$\frac{\partial}{\partial t}(\rho \omega) + \frac{\partial}{\partial x_i}(\rho \omega u_i) = \frac{\partial}{\partial x_j}\left(\Gamma_\omega \frac{\partial \omega}{\partial x_j}\right) + G_\omega - Y_\omega \quad (6)$$

In these equations, G_k represents the generation of turbulence kinetic energy due to mean velocity gradients. G_ω represents the generation of ω. Γ_k and Γ_ω represent the effective diffusivity of k and ω, respectively. The terms Y_k and Y_ω represent the dissipation of k and ω due to viscous effects. A detailed description of the model and the associated empirical parameters may be found in the Theory Guide (ANSYS, 2009) of ANSYS Fluent.

2.2 Grid Generation and Computational Domain

The computational domain contains only the internal structures of the melt blowing device as shown in Figure 3. The average diameter of the polymer filament is around 10 micrometers, which is negligible compared with the scale of the flow field, so the polymer material nozzle and the related structure is removed from the CAD model. Since the dimension along the X-direction of the MB device is quite large compared with other two dimensions and the internal structure maintains a periodic pattern, we assume flow in this direction is also periodic with the same period as the structure pattern.

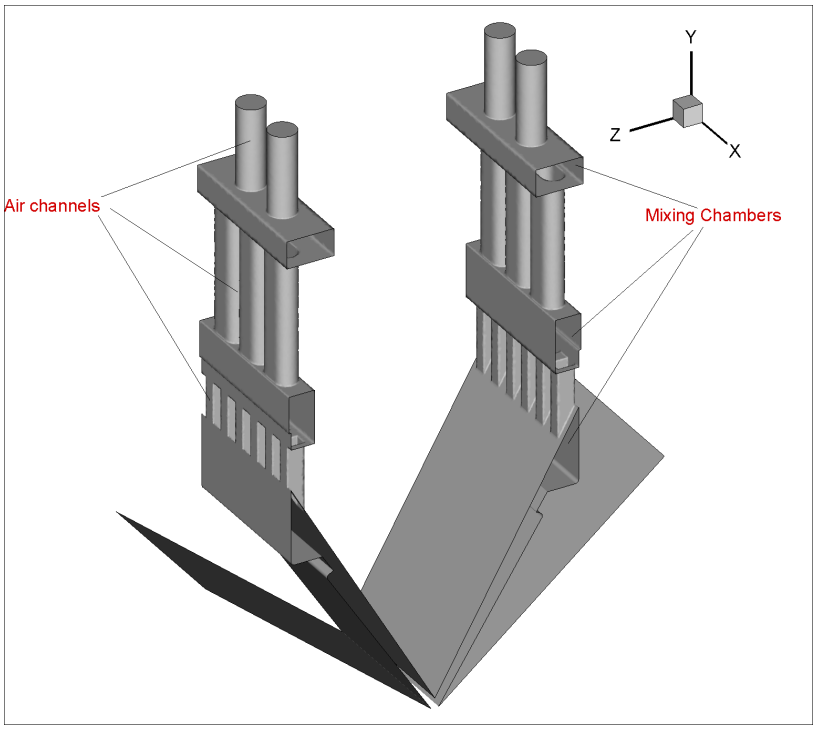

Figure 3 - CAD model of the computational domain

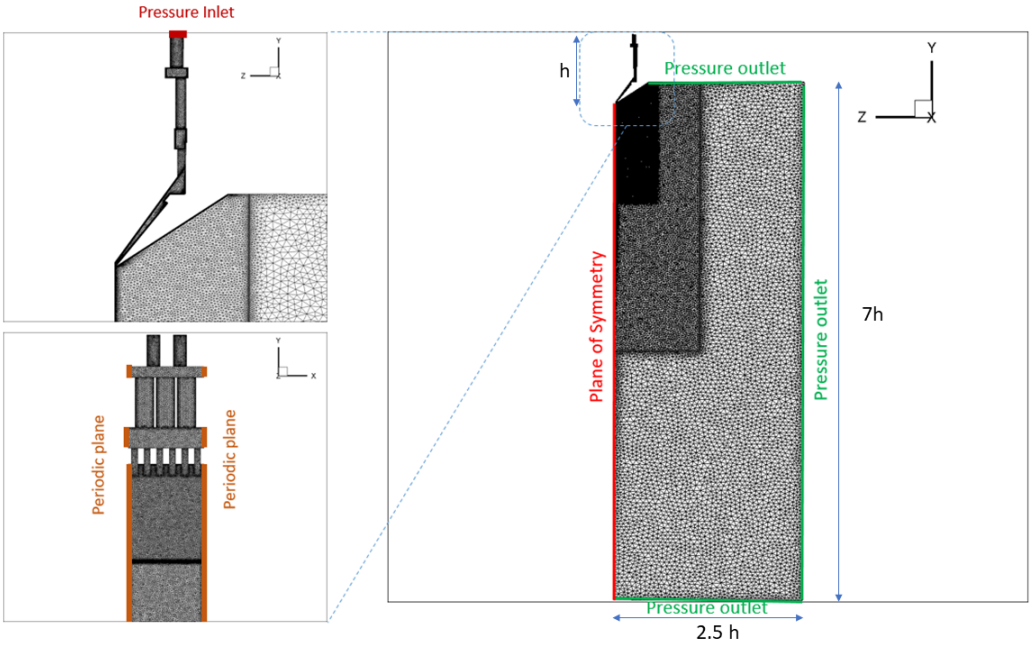

Figure 4 - Computational domain and boundary condition for the baseline setup

The computational domains of all cases were generated using Pointwise V18.0R2. Figure 4 represents the computational domain used in the simulation for the baseline case setup. The origin of the die body is at the center of the die tip, with z-direction traversing the major slot axis; the y-direction is the downward direction below the die. The x-direction is perpendicular to the plane of the drawing. The domain dimensions were 300mm and 1000 mm in the z-direction and y-directions, respectively. These dimensions are large enough to represent the air velocity and temperature profiles below the die. The diameter of the polymer is between 0.1 and 10 micrometers, and its influence on the flow field was considered negligible. A symmetry boundary condition was used along the y-axis ($z = 0$) to reduce the size of the computational domain.

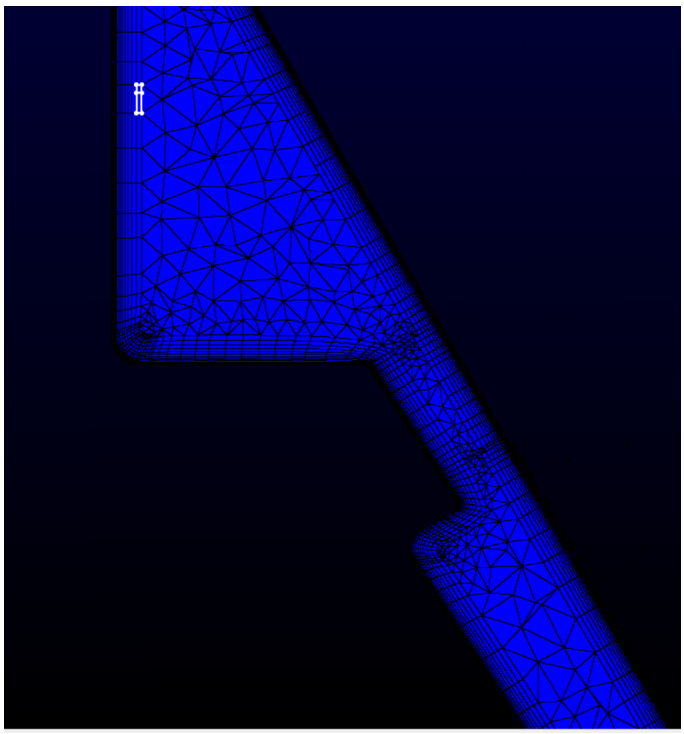

Figure 5 - T-rex grid in the mixing channel and air plate

As shown in Figure 3, the complex internal structure makes it difficult to get a high-quality structured grid. The sharp edge near the die tip and the internal mixing channel will result in cells with a high level of skewness, compromising the solution accuracy. An unstructured tetrahedral grid can overcome this difficulty. The disadvantage of the unstructured grid topology is the significant increase in the number of grid points, requiring greater computing resources in terms of memory and computer time. Since the majority computational domain in our study is for internal flow, we use a hybrid meshing hexahedral-tetrahedral mesh, using the unstructured grid only where needed. Pointwise V18.0R2 provides a feature called T-Rex grid, as shown in Figure 5. T-Rex generates hybrid meshes that resolve boundary layers, wakes, and other phenomena in viscous flows by extruding layers of high-quality, high aspect ratio tetrahedra that can be post-processed into stacks of prisms (denoted by the white outline in Figure 5). The algorithm includes tools for optimizing cell quality. The grid is unstructured with tetrahedral cells out of the boundary and quadrilateral cells inside the boundary layer region. This results in fewer grid points in the boundary layer region. The grid resolution of the area that is close to the symmetry plane and the die tip is resolved with a very fine grid, and the grid becomes coarser farther away from the die tip. The total number of computation cells was around 3,000,000.

2.3 Boundary and Initial Conditions

The melt blowing process simulated in this research is based on a real world paper making industry process (Haynes, B. D & Cook, 2005). All the boundary and initial conditions setup are chosen to correspond to the real-world industrial conditions as shown in Table 1.

Table 1 Boundary conditions

Boundary condition type	Boundary condition parameters
Pressure Inlet	T = 500 K, P = 3.5 psi (gauge)
Pressure Outlet	T = 300 K, P = 0 psi (gauge)
Isothermal wall	T = 300 K

The air flow entering the computational domain was set as a pressure inlet boundary condition at $T = 500K$ and $P = 3.5\ psi$. The right and the bottom boundary (see Figure 4) were set as pressure outlets with ambient air conditions ($T = 300\ K$ and $P = 0\ psi\ (gauge)$). The left plane was set as a symmetric plane. All surfaces denoted in orange color (see Figure 4) are set as periodic boundaries to satisfy the periodic flow assumption in x-direction. All solid boundaries were assigned the default setting of wall at a temperature equal to $300K$. The turbulence parameters were set with a length scale of 0.001 m at the inlet and with a turbulence intensity of 5%. The turbulence at outlet was set with a length scale of 1 m and with an intensity of 1%. These values have been estimated based on experimental results. The air flow was modeled as a compressible flow and its density ρ were calculated using ideal gas law and the viscosity μ was calculated using Sutherland law described below:

$$\mu = \frac{C_1 T^{3/2}}{T + C_2} \tag{7}$$

Where T is the static temperature in K. For air at moderate temperatures and pressures, $C_1 = 1.458 \times 10^{-6}$, and $C_2 = 110.4\ K$.

2.4 Fluent Solver Setup

In ANSYS FLUENT, two solver technologies are available (ANSYS, 2009). They use different algorithm and strategies to solve the continuity, momentum and energy equations. A pressure-based solver was widely used to solve the incompressible and flows and low-Mach-number compressible flows, or loosely speaking, the low-speed incompressible flows. A density-based solver is also available for high-speed compressible flows. Both approaches yield good results (Chen & Przekwas, 2010). The only difference is the speed at which the solution converges to a nominally steady flow with limit cycle oscillations.

In the present study, the jet speed near the die tip is close to 210 m/s, and the local Mach number is 0.7, and the flow field in the internal structures are much slower but still has a Mach number around 0.3. Much of the flow is compressible From previous studies (Miettinen & siikonen, 2015), the density based solver has a greater convergence speed than the pressure-based solver for the compressible flow. Based on the discussion above, the density solver was chosen in the present simulations.

The density-based solver in the ANSYS FLUENT solves the governing equations of continuity, momentum, and energy equation together. Since the governing equations are

non-linear and coupled, several iterations of the solutions of the solution loop will be performed before a converged solution is obtained. Figure 6 illustrates the steps for the solver iterations.

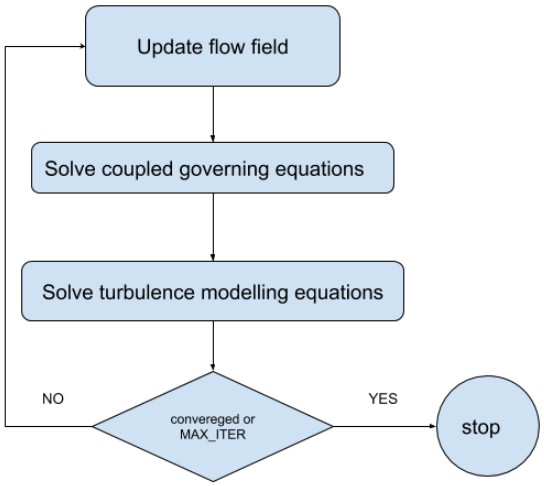

Figure 6 - Steps for the density-based solver algorithm

2.5 Fluctuation Reduction Devices and Porous Media Conditions

A porous media model is available in FLUENT and maybe used for a wide variety of single phase and multiphase problems, including flow through packed beds, filter papers, perforated plates, flow distributors, and tube banks. In this study, this model was used to model the two proposed flow fluctuation reduction devices- wire mesh screen and honeycomb. We first define a cell zone in which the porous media model is applied, and the pressure loss in the flow is determined via the sum of viscous resistance and inertial resistance. An one-dimensional simplification of the porous media model, termed the "porous jump" can be used to model a thin membrane with known velocity/pressure-drop

characteristics. The porous jump model is used to model the screen mesh, whereas the porous zone model is used to model the honeycomb.

The porous media models for single phase flows and multiphase are modeled by the addition of a momentum source term to the standard fluid flow equation. The source term is composed of two parts: a viscous loss term (Darcy, the first term on the right-hand side of Equation (8), and the inertial loss term (the second term).

$$S_i = \left(\sum_{j=1}^{3} D_{ij} \mu v_j + \sum_{j=1}^{3} C_{ij} \frac{1}{2} \rho |v| v_j \right) \tag{8}$$

Where, S_i is the source term for the ith momentum equation, $|v|$ is the magnitude of the velocity and D and C are prescribed matrices. This momentum sink contributes to the pressure gradient in the porous cell, creating a pressure drop that is proportional to the fluid velocity in the cell.

In the case of a simple homogeneous porous medium, equation (9) simplifies to

$$S_i = -(\frac{\mu}{\alpha} v_i + C_2 \frac{1}{2} \rho |v| v_i) \tag{9}$$

Where α is the permeability and C_2 is the inertial resistance factor, simply specify D and C as diagonal matrices with $1/\alpha$ and C_2, respectively, on the diagonals (and zero for the other elements).

2.5.1 Wire Mesh Screen Setup

It is well known that a mesh screen placed across an airflow will have a smoothing effect, distributing both the velocity and pressure across the screen. A typical wired stainless steel mesh screen device has been quantified before (Kimberly Clark Coraporation, 2000), as shown in Figure 7. The pressure drop and velocity change have been related to the mesh wire diameter, mesh number, and the wire spacing. The following empirical relation was used:

$$\mathrm{P} = \frac{\mathrm{V}^{1.5}}{42.8 * 10^{2.59A}} \tag{10}$$

Where P is the screen pressure, V is the velocity and A is the free hole area which is a fixed value depending on the type of the steel mesh screen. The geometry parameters of the mesh screen we modeled in this study is listed in Table 2.

Table 2 Wire mesh screen parameters

Wire Diameter (inches)	0.0045
Mesh Number (wires /inch)	100
Wire Spacing (inches)	0.0055
Free Hole Area	30.3%

Inspired by this property of the mesh screen, porous jump conditions are used to model the wire mesh screen, which has known velocity (pressure-drop) characteristics. It is

essentially a 1D simplification of the porous media model available for cell zones. The thin porous medium has a finite thickness over which the pressure change is defined as a combination of Darcy's Law and an additional inertial loss term:

$$\Delta p = -\left(\frac{\mu}{\alpha} v + C_2 \frac{1}{2} \rho v^2\right) \Delta m \tag{11}$$

Where μ is the laminar fluid viscosity, α is the permeability of the medium, C_2 is the pressure-jump coefficient, v is the velocity normal to the porous face, and Δm is the thickness of the medium. In our case, Δm is the diameter of the wire. Appropriate values for α and C_2 was calculated using curve fitting (Figure 8) based on the Equation (11) and Table 2.

Table 3 Porous media pressure-jump interface setup in Fluent

Face Permeability α	5.56×10^{-10}
Porous Medium Thickness Δm	0.000143
Pressure-Jump Coefficient (C2)	94035
Thermal Contact Resistance	0

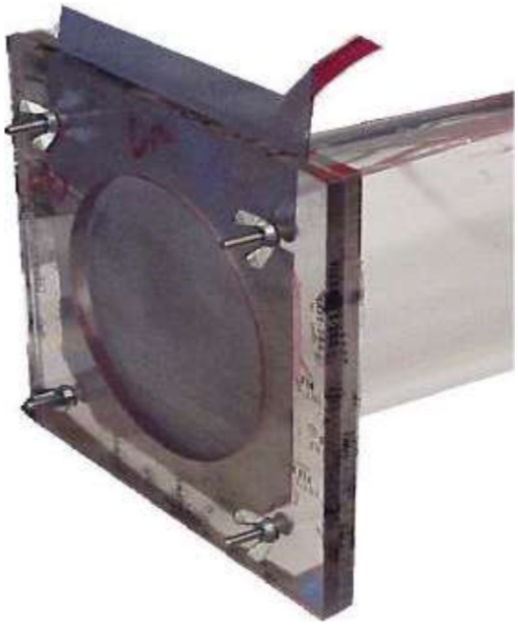

Figure 7 - Wire mesh screen in a test setup

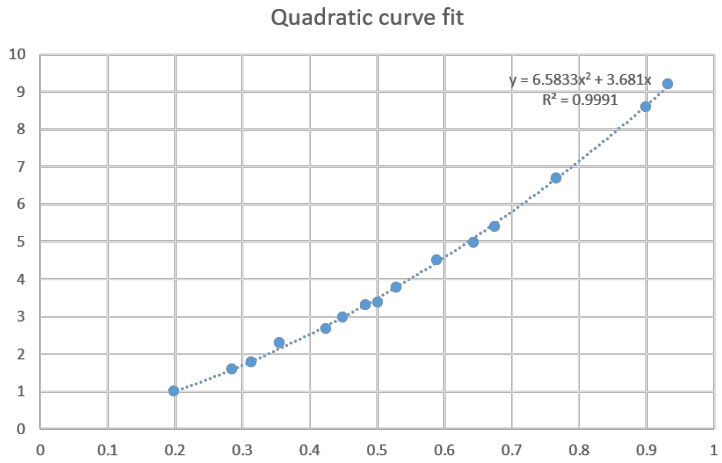

Figure 8 - Curve fitting for the wire mesh screen setup

Since the porous jump model is a 1D simplification of the porous media model, the porous-jump zone must be modeled as the interface between cells, rather than a cell zone. According to the results of industrial experiments (Kimberly Clark Coraporation, 2000), the best location to reduce the upstream velocity fluctuation is shown in Figure 9.

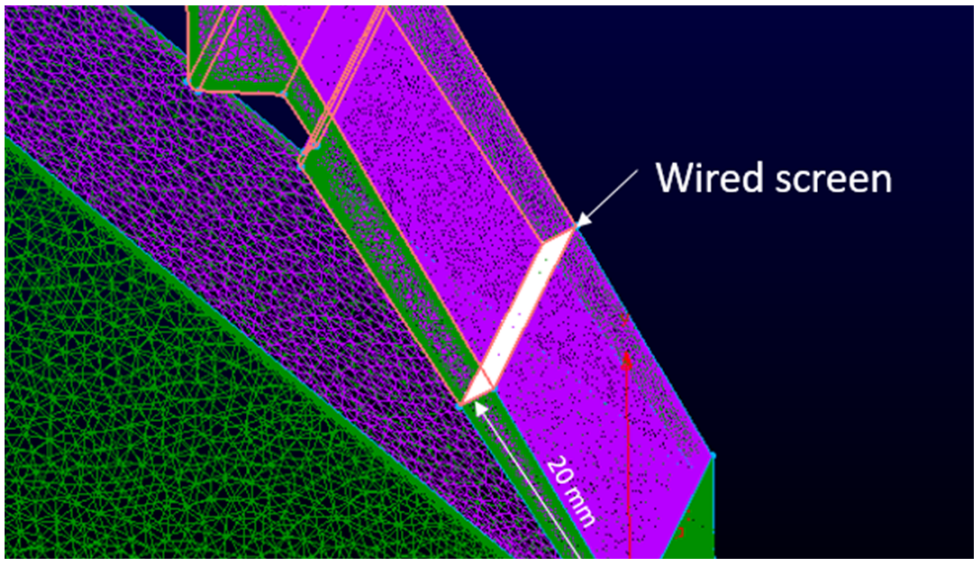

Figure 9 - Location and setup of wire mesh screen

2.5.2 Honeycomb Setup

The wire mesh screens reduce the longitudinal components of turbulence or mean-velocity variation to a greater extent than the lateral components. To get more flow straightening and turbulence reduction, honeycomb has been widely used in wind tunnel design and across different industrial areas, as shown in Figure 10 (ARA, 2017). Honeycomb is one kind of filter used to constrain flow in one direction and filter out the large scale of vortex structures. The function of honeycomb with different length and width in improving flow quality were studied by (Li, Liu, & Cheung, 2013). With the presence of the honeycomb, the lateral distribution of longitudinal mean velocity and the turbulent intensity both decayed in the downstream.

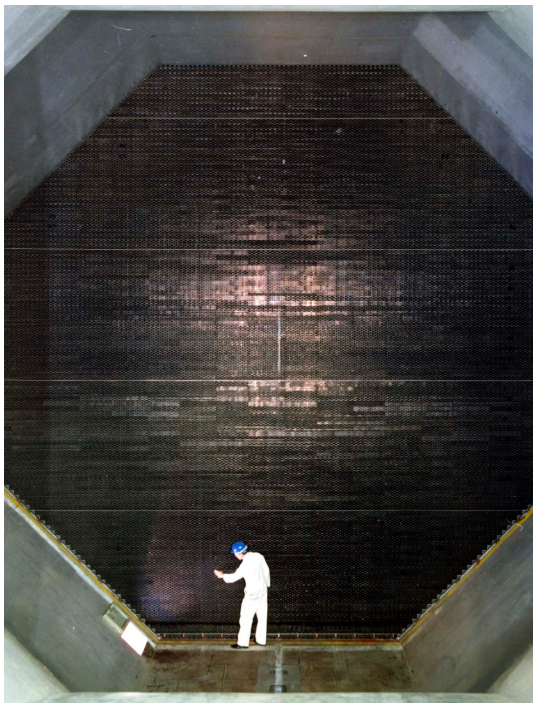

Figure 10 - TWT honeycomb flow straightener in the ARA wind tunnel

In ANSYS FLUENT the behavior of the honeycomb can be mimicked by defining the porous media zone. The pressure-drop that ANSYS FLUENT computes in each of the three (x, y, z) coordinate directions with the porous region is then:

$$\Delta p_x = \sum_{j=1}^{3} \frac{\mu}{\alpha_{xj}} v_j \Delta_{n_x} \tag{12}$$

$$\Delta p_y = \sum_{j=1}^{3} \frac{\mu}{\alpha_{yj}} v_j \Delta_{n_y} \tag{13}$$

$$\Delta p_z = \sum_{j=1}^{3} \frac{\mu}{\alpha_{zj}} v_j \Delta_{n_z} \tag{14}$$

Where $1/\alpha_{ij}$ are the entries in the matrix D in Equation (9), v_j are the velocity components in the x, y and z directions, and $\Delta n_x, \Delta n_y$, and Δn_z are the thickness of the medium in the x, y and z directions. Here, the thickness of the medium ($\Delta n_x, \Delta n_y$, and Δn_z) is the actual thickness of the porous region in our implementation.

At high flow velocities, the constant C_2 in the Equation (10) provides a correction for inertial losses in the porous medium. This constant can be viewed as a loss coefficient per unit length along the flow direction, thereby allowing the pressure drop to be specified as a function of dynamic head, written in terms of the pressure drop in x, y, z directions:

$$\Delta p_x \approx \sum_{j=1}^{3} C_{2_{xj}} \Delta n_x \frac{1}{2} \rho v_j |v| \tag{15}$$

$$\Delta p_y \approx \sum_{j=1}^{3} C_{2_{yj}} \Delta n_y \frac{1}{2} \rho v_j |v| \tag{16}$$

$$\Delta p_z \approx \sum_{j=1}^{3} C_{2_{zj}} \Delta n_z \frac{1}{2} \rho v_j |v| \tag{17}$$

Again, $\Delta n_x,\ \Delta n_y, and\ \Delta n_z$ are the thickness of the medium in the $x, y, and\ z$ directions. ANSYS FLUENT solves the standard energy transport equation in porous media regions with modifications to the conduction flux and the transient terms only. The details of this part can be found in (ANSYS, 2009).

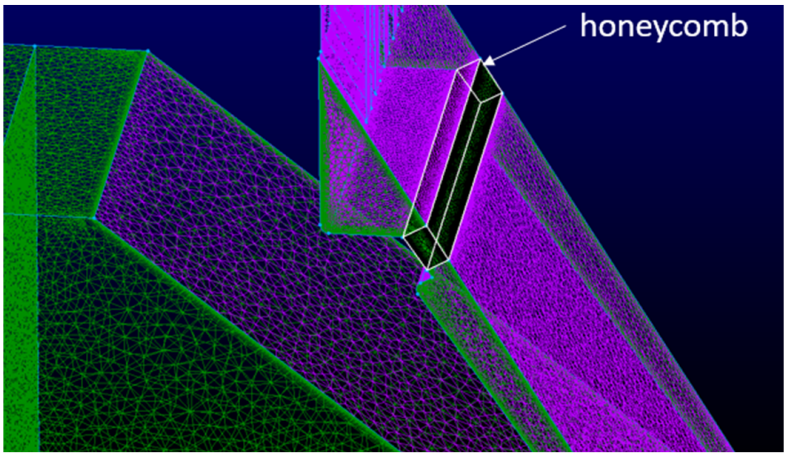

Figure 11 - Honeycomb location and parameters setup

In ANSYS FLUENT, the standard conservation equations for turbulence quantities were solved in the porous medium. Turbulence in the medium is treated as though the solid medium does not affect the turbulence generation or dissipation rates. This assumption may be reasonable if the medium's permeability is quite large and the geometric scale of the medium doesn't interact with the scale of the turbulent eddies.

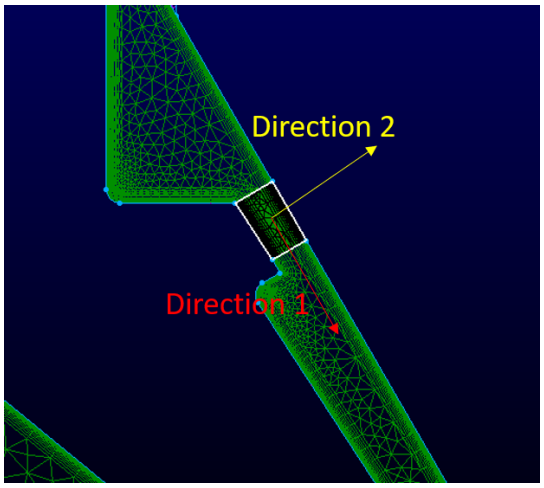

Figure 12 - Directions annotation of the honeycomb porous media zone

The honeycomb is installed between the last mixing chamber and jet channel Figure 11. To reduce the velocity fluctuation in the x-direction, the inertial and viscous resistance in the x-direction, or direction-1 annotated in Figure 12 and the direction perpendicular to the air plate are set to be 10^3 larger compared with the flow direction along the air channel.

Table 4 Porous medium zone setup for honeycomb

Relative velocity resistance (Direction-1)	3.84×10^7
Relative velocity resistance (Direction-2)	3.84×10^{10}
Relative velocity resistance (Direction-3)	3.84×10^{10}
Initial Resistance (Direction-1)	20.414
Initial Resistance (Direction-2)	20414
Initial Resistance (Direction-3)	20414

The parameters setup for honeycomb porous media zone was based on the pressure jump of the wire mesh screen. All the parameters of the porous medium zone found in Table 4 were chosen to make the pressure jump very close to the wire mesh screen case, so the jet speed and the flow field in down screen can be compatible for both cases. Because of the increasing of viscous resistance, the Reynolds number will decrease, so we simply imply that μ_t is zero and that generation of turbulence will be zero in this porous media zone.

CHAPTER 3. RESULTS AND DISCUSSIONS

3.1 Baseline Case Study

The baseline case was used to understand and identify the sources of unsteady flow at the jet exit. Since this study is based on a real industry device and the internal flow experiment data is not available for the comparison, this study was performed by analyzing the flow field through time series analyses and flow visualization. The process consists of three parts:

- Examine the velocity magnitude and TKE contour of the special locations of the internal structures; verify whether the flow field is captured with enough number of points and if the flow is adequately evolved.
- Examine the flow field pattern in the x-direction to verify whether the periodic boundary condition is applied properly.
- Use point measurements in the air channel and jet flow field to analyze the time series of the velocity field and identify regions where maximum velocity fluctuations occur.

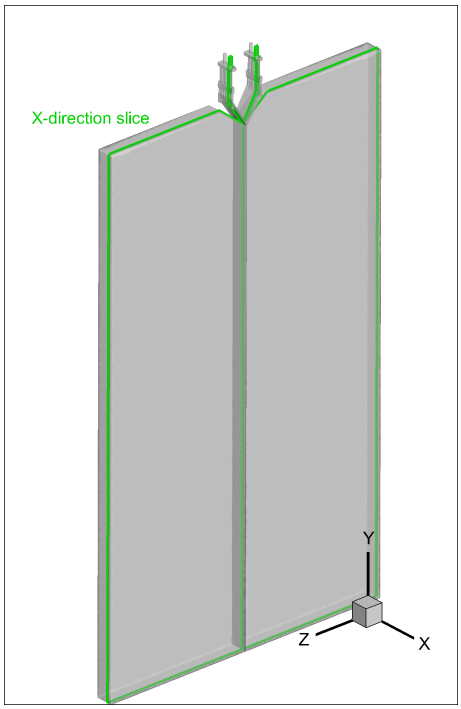

Figure 13 - Location of the x-direction slice

3.1.1 Flow Field Analysis

The jet flow field is critical to the melt blowing process as discussed earlier. The materials filaments are extracted by the high-speed imping jets. A temporally steady flow field is desired for best results from the melt-blowing process. To visualize the flow field in the whole domain, a x-direction slice was used as shown in Figure 13. Figure 14 shows velocity and turbulent kinetic energy (TKE) contours on the x-direction slice. We can observe that the jet is fully developed. The velocity magnitude contour (left) clearly shows the free shear layer created by the jet flow. The TKE contour (right) has a high magnitude near the die tip and as the jet propagate downstream, the TKE level along the centreline decreases. This is caused by reduction in the vorticity magnitude (which controls TKE production), and dissipation of TKE.

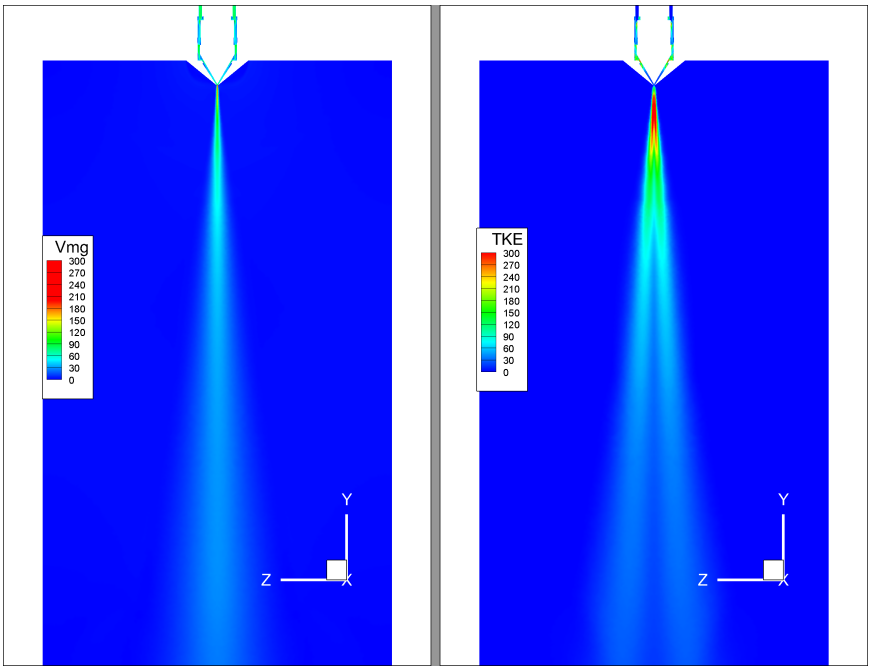

Figure 14 - Jet flow field of the baseline case

The baseline case is next studied to investigate the mechanisms of the flow oscillations. The complex geometry of the mixing chamber and the air channels, with their sharp corners and sharp turning angles, give rise to flow separation and vortex shedding. These are two of the main reasons for the self-triggered flow oscillations at the jet exit. Figure 15 shows the velocity magnitude contours and TKE contours within the air channels. The blue clor in the velocity magnitude contours denotes the vortex zone with low velocity, which appears at the sharp corner of each mixing chamber and at the the backward steps of the air plates. Also, in Figure 14 we can see higher TKE in these regions.

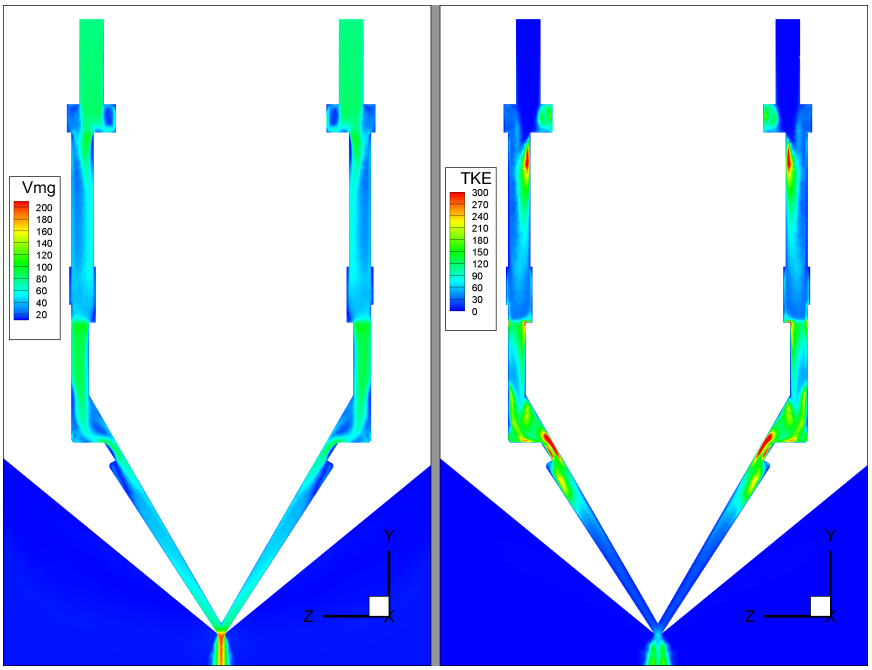

Figure 15 - Velocity and TKE magnitude contour plots

The velocity vectors plots are additional useful tools for visualizing the flow structures and showing flow reversal in the air mixing chambers. The color of the velocity vector denotes the velocity magnitude. In the mixing chamber and corners of air channels, we can observe some vortex structures caused by the flow separation, which is consistent with the velocity magnitude in Figure 16. These flow structures are unstable because of the inflection point in the velocity profile. The inflection point would trigger transition of the flow from laminar to turbulent flow.

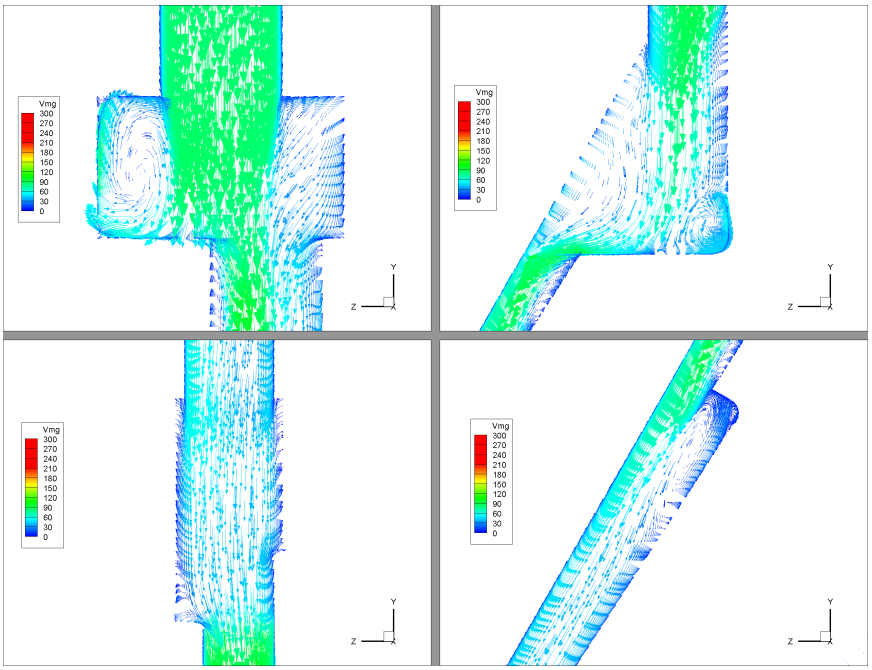

Figure 16 - Velocity vector plots in the mixing chambers

Another very important problems we would like to overcome is the flow inhomogeneity in the x-direction. Slices along the y-direction were used to study the flow field in the different mixing zones and air channels, as shown in Figure 17. The velocity magnitude of slices side by side in Figure 18 and the TKE contours are shown in Figure 19. The slices from left to right are in an ordered of the flow direction from the inlet to the downstream.

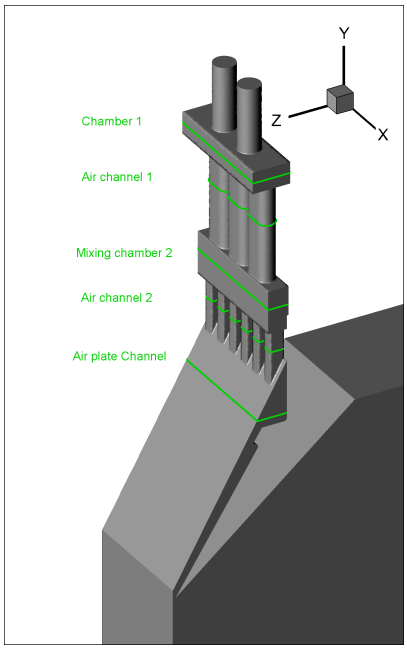

Figure 17 - Location of the y-direction slices

If we only look at the mixing chamber 1, chamber 2 and air plate channel, we can see those three structures were designed to reduce the flow pattern caused by the air channels in the upstream. For example, in the mixing chamber 2, the velocity magnitude shows three cylindrical circles with locally high magnitude. These are caused by the air channel 1. The TKE contours also show similar higher magnitude area although the edge of the cylinders was smeared out.

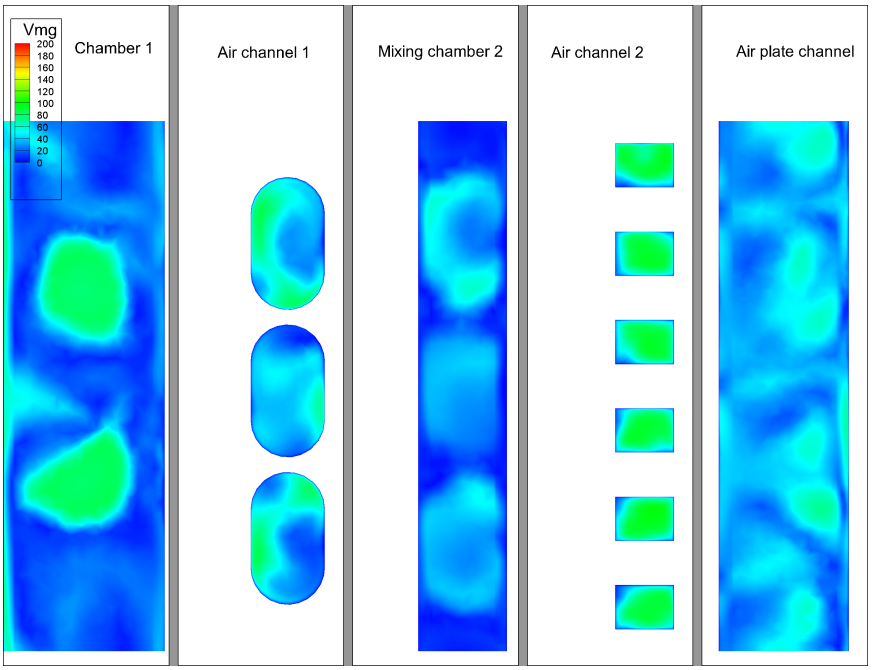

Figure 18 - Velocity magnitudes on y = constant planes

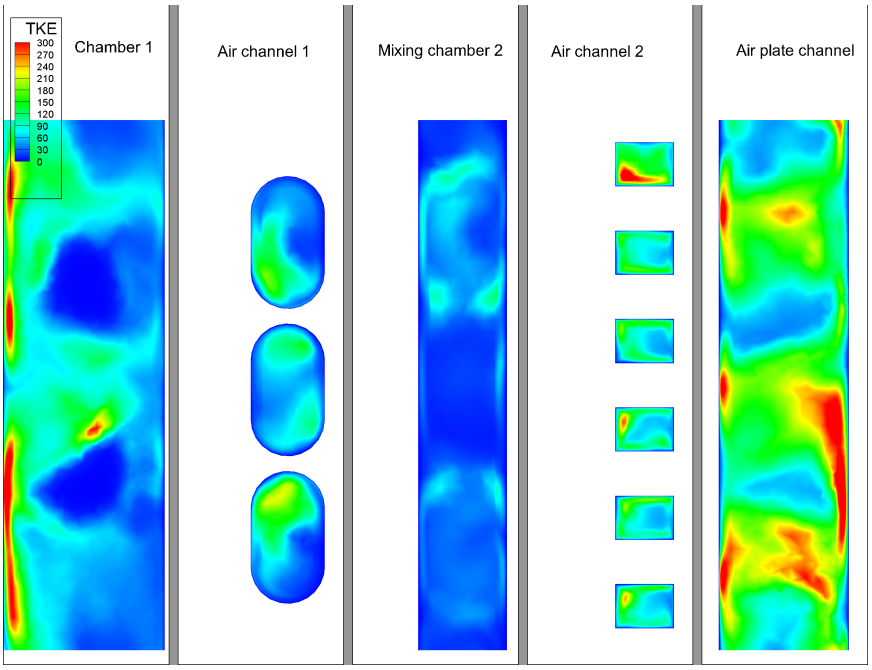

Figure 19 - TKE contours on y = constant planes

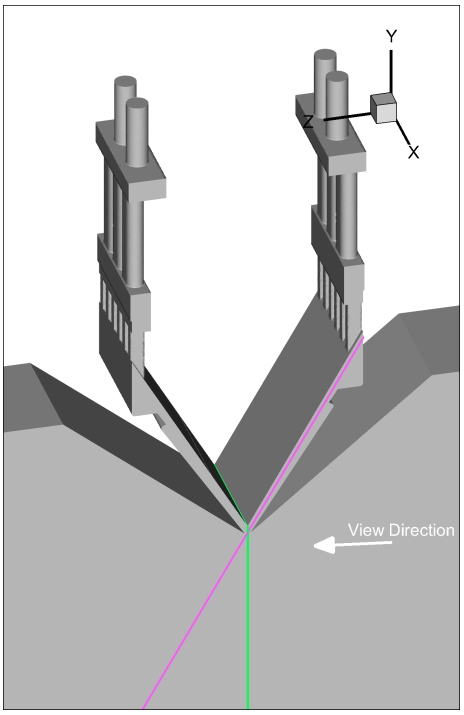

Figure 20 - Location and the view direction of the Z-direction slices

The flow filed was also examined on z= constant planes as shown in Figure 20. Figure 21 shows the velocity magnitude contours and the TKE contours on a representative Z= Constant plane. We can see that the flow pattern in the air channel significantly affects the flow in the jet. The high-speed air flow from air channel 2 propagates to the downstream jet flow region, causing the jet flow to be inhomogeneous in the x-direction as we already discussed before. In addition to the spikes seen in the velocity magnitude in the high-speed jets region, the TKE contour also shows some interesting prosperities. We can observe three large spikes in the jet flow region, and these are associated with the flow from the air channel 1. Thus, the upstream structures are strongly influence the flow field downstream.

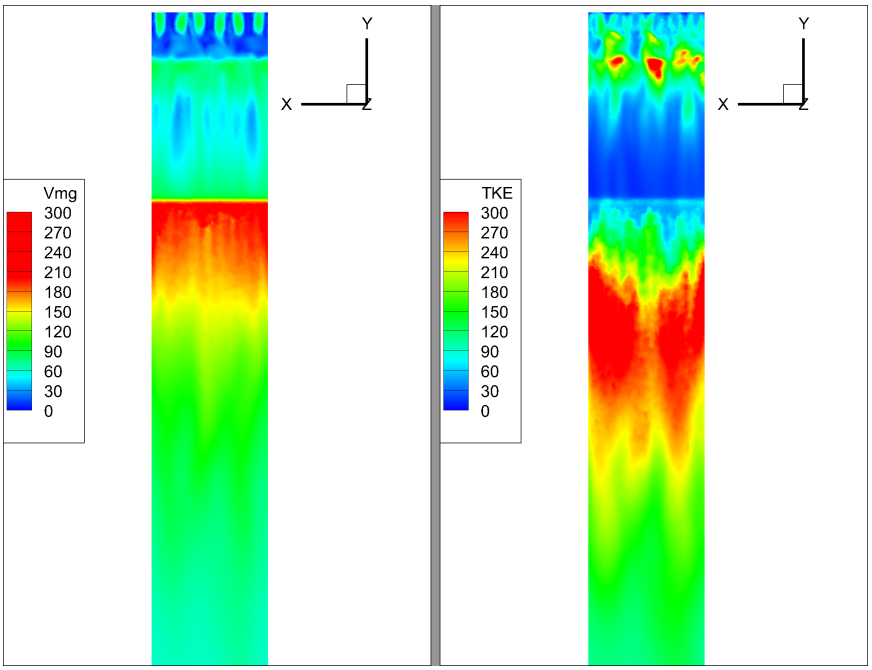

Figure 21 - Velocity and TKE contours on a z = constant planes

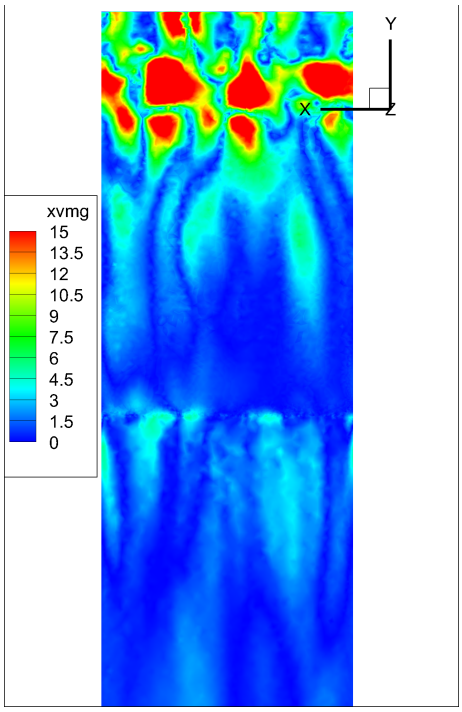

Figure 22 - X-component of the velocity

Figure 22 indicates that there is significant flow (10% of the velocity magnitude) along the x- direction. If the jets were truly parallel to each other, this component of velocity would be negligibly small. The higher magnitude of the magnitude indicates that the jets interact with each other. Figure 23 shows the path lines of the internal flow of the whole system on an x-y plane. The path lines are tangled with each other in the air channels and mixing chambers, and also cross each other in the air plate channel and in the jet flow region. This cross-flow will the polymer filaments to move laterally and become tangled with each other, affecting the quality of the fiber product.

Figure 23 - Path line plot for the baseline case

3.1.2 Velocity Time Series Analysis

To further investigate the unsteady flow field. Time history of the flow field was tracked at a number of locations as shown in Figure 24.

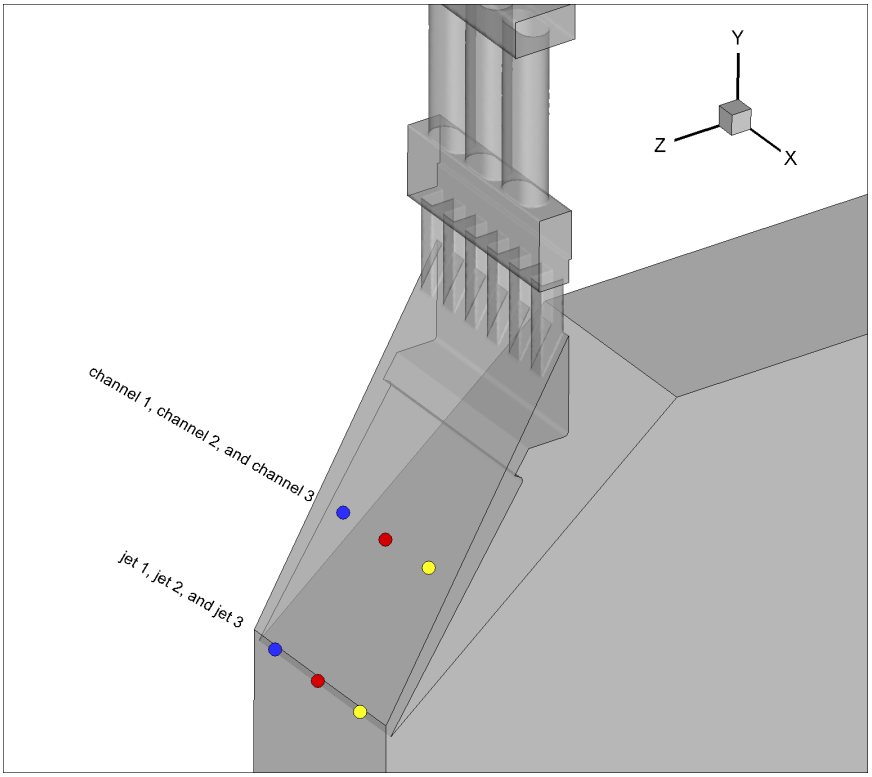

Figure 24 - Location and the name of the time series point measurements

To normalize all the point measurements, the following post-processing was done:

$$V_{norm} = \frac{V_{mag}}{Avg(V_{mag})}$$

Figure 25 shows the time history of the normalized velocity. It is seen that the velocity oscillation at three locations are not correlated with each other. We can also see that the magnitude of the velocity fluctuations dramatically decreases in the jet flow region.

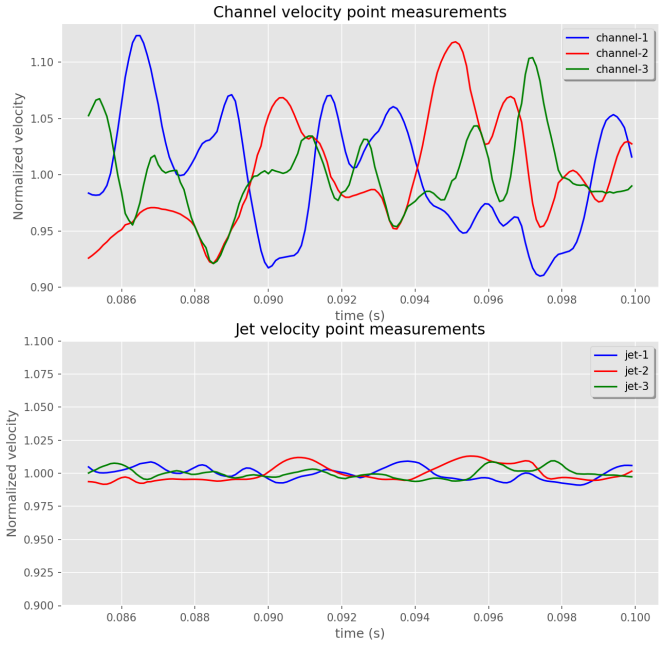

Figure 25 - Velocity time series of point measurements

To study the time series data in the frequency domain, the Power Spectrum Density (PSD) plots, shown in Figure 26, was generated. The top row is the plots of PSD of in channels 1, 2 and 3, while the bottom row is the PSD for corresponding jet point measurements. We can see the dominant frequencies are nearly the same for each pair of channel and jet points, indicating the oscillation patterns in the upstream region propagate to the downstream jet region. Since the dominant frequency is low, the jet will oscillate over a relatively long period, which is consistent with the frequency of the separation bubble formation and detachment upstream. Cross-correlation coefficients were used to illustrate the overall influence of the upstream unsteadiness on the downstream, as shown in Figure 27. We can see that the main diagonals (Channel-Jet pair) has the largest R-value (i.e. correlation coefficient). Thus, we can conclude that the upstream flow pattern is well correlated with the unsteady flow at the jet exit.

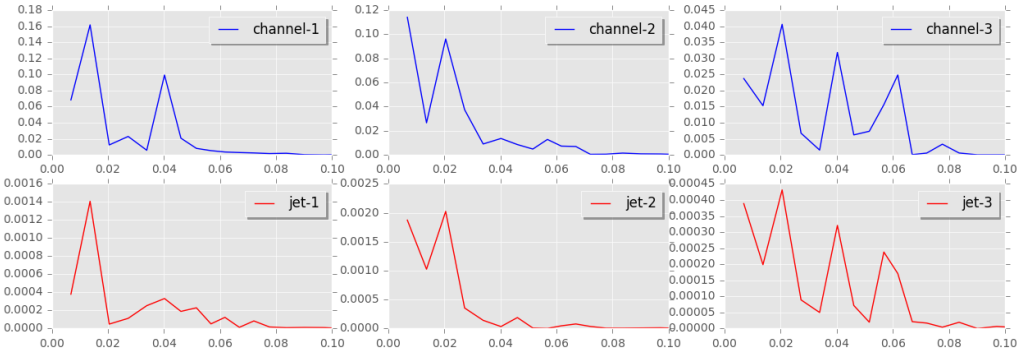

Figure 26 - PSD plots of velocity time series

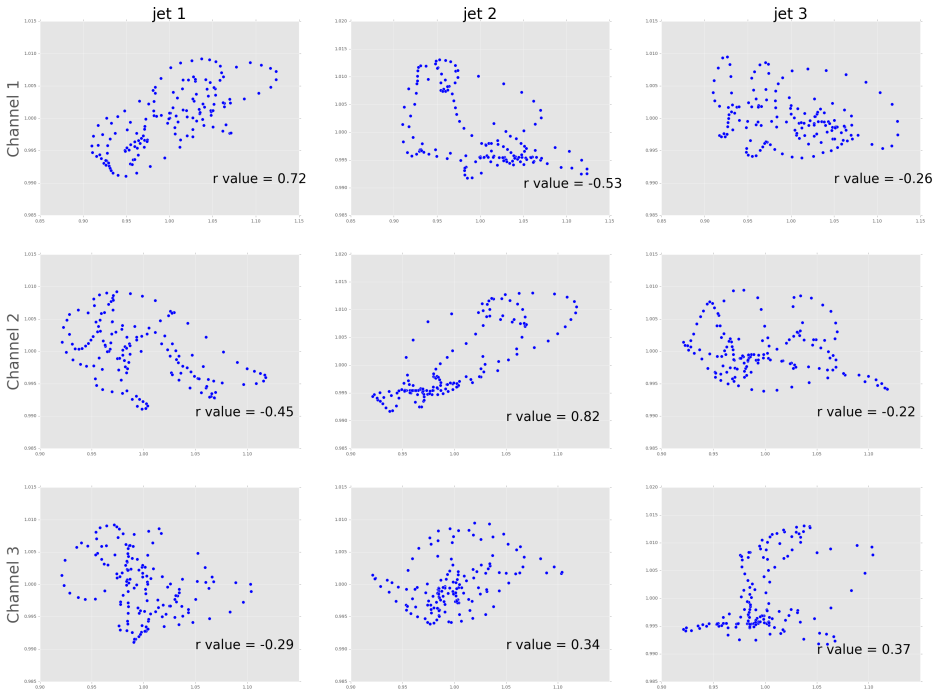

Figure 27 - Cross-correlation coefficients of time series point measurements

3.2 Effect of the Wire Mesh Screen

Mesh screens are widely used in wind tunnels to reduce the upstream flow inhomogeneity and turbulence intensity. In the present study, we investigate how a mesh screen placed upstream will affect the flow properties in the jet region. The blockage caused by the screen would reduce the flow rate. To compensate for this, the upstream pressure was raised slightly, preserving the same oveall mass flow rate as the baseline case. The effect of the mesh screen was studied immediately downstream of the mesh screen as shown in Figure 28.

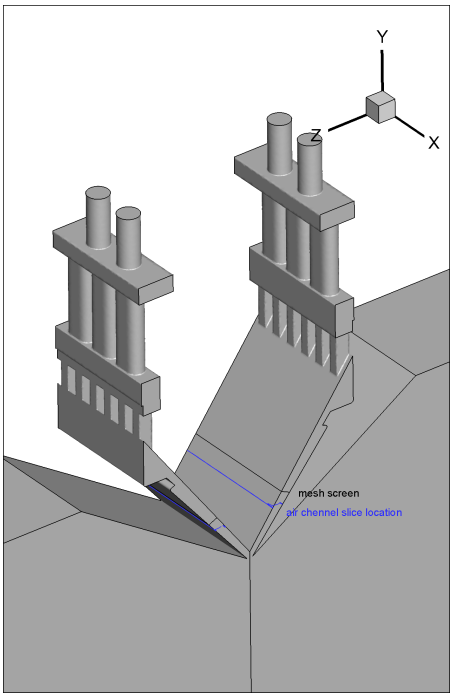

Figure 28 - Location of the air channel slice

3.2.1 Velocity Magnitude and TKE Contour Analysis

Figure 29 shows the velocity magnitude contours in the air plate channel downstream of the mesh screen. With the presence of wire mesh screen, the flow field looks more even than the baseline case (also shown), and the velocity magnitude doesn't

decrease too much. According to Darcy's law (Equation 8), the pressure jump across the porous media screen is proportional to V^2, so the high velocity area will be slow down with higher negative pressure gradient and then smooth the flow field.

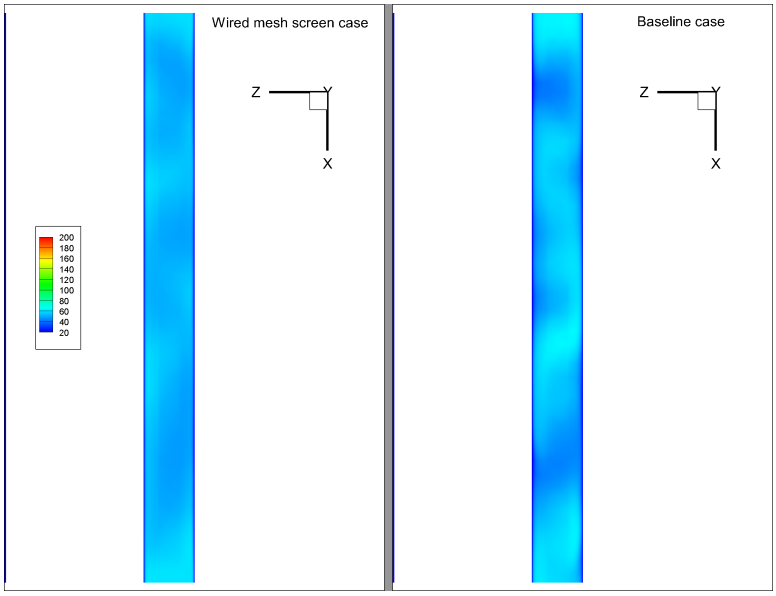

Figure 29 - Velocity magnitude contours in the air channel behind the mesh screen

The TKE contour within the air plate channel downstream of the mesh screen is shown in in Figure 30. It is seen that the screen lowers the TKE compared to the baseline case (right).

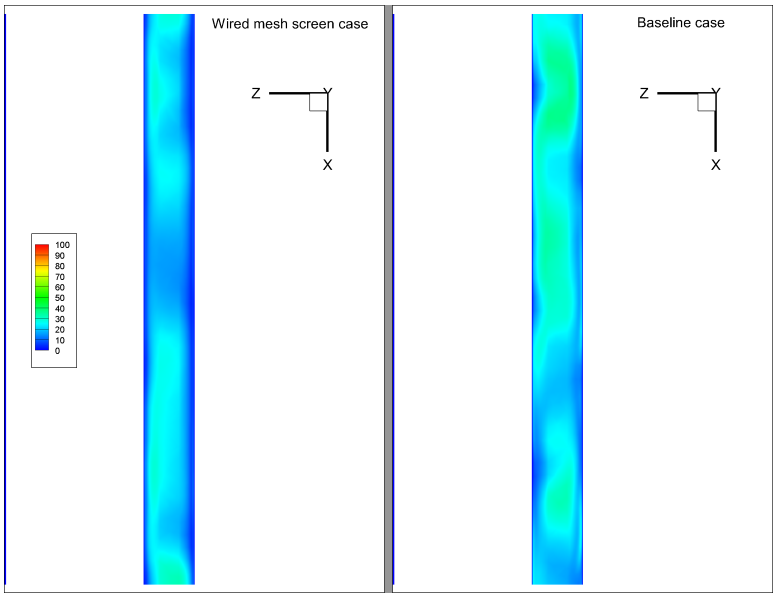

Figure 30 - TKE contour in the air channel behind the mesh screen

We also examine the effect of the wire mesh screen on the jet flow field below the die tip. To visualize the flow field in the air channel, we use the same Z-= Constant slice as shown in Figure 20. The comparison of velocity magnitude contours with and without the mesh screen is shown in Figure 31. Compared with the contour plot on the right (baseline case), the velocity magnitude field is smoother, and the edges of the low speed (blue) region are blurred across the wire mesh screen. The TKE contours shown in Figure 32 shows that the TKE level was reduced by the wire mesh screen and that the jet flow field has smaller spikes compared to the baseline case.

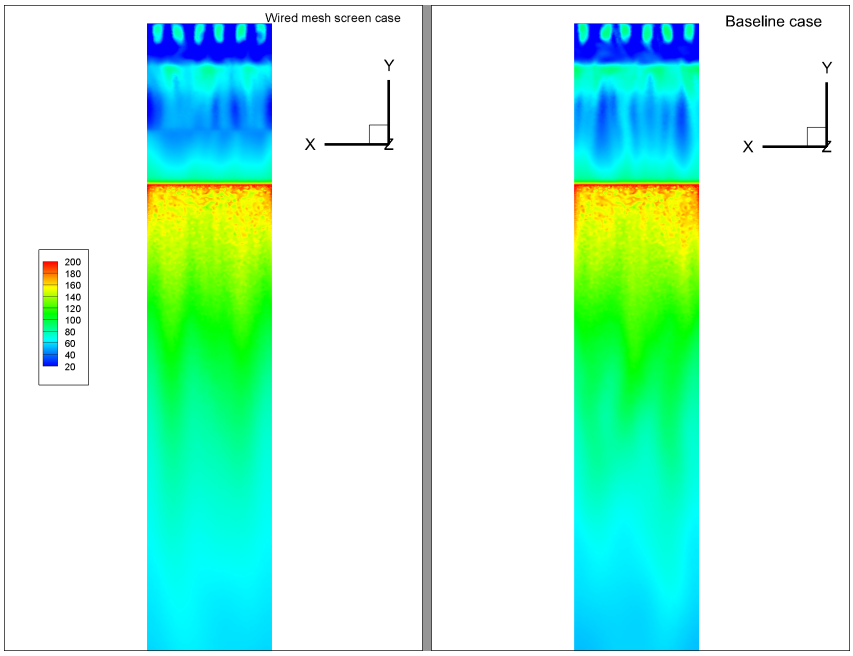

Figure 31 - Velocity magnitude contour comparison between wire mesh screen (left) and baseline (right)

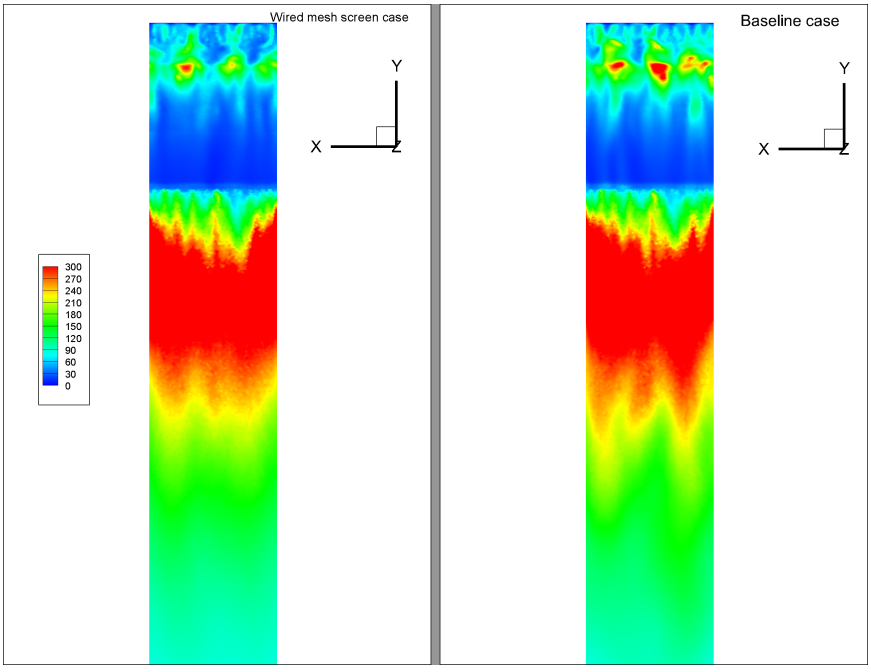

Figure 32 - TKE contour comparison between wire mesh screen case (left) and baseline case (right)

From these visualizations, we can conclude that with the use of the wire mesh screen the downstream flow is more evenly distributed in the X-direction. The wire mesh screen does help reduce the level of inhomogeneity across the jet flow to some extent.

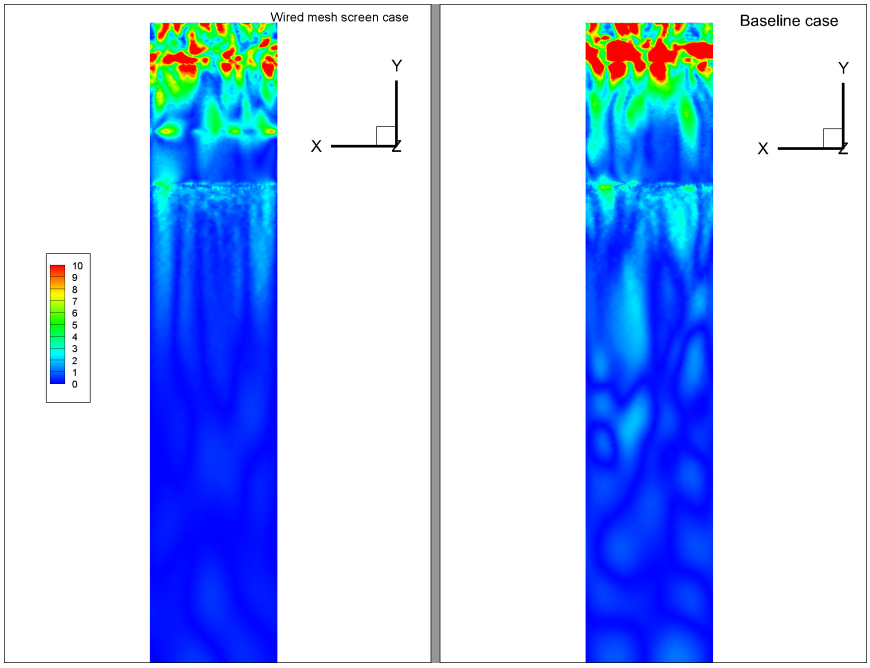

Figure 33 - X-Velocity magnitude comparison between wire mesh screen case (left) and baseline case (right)

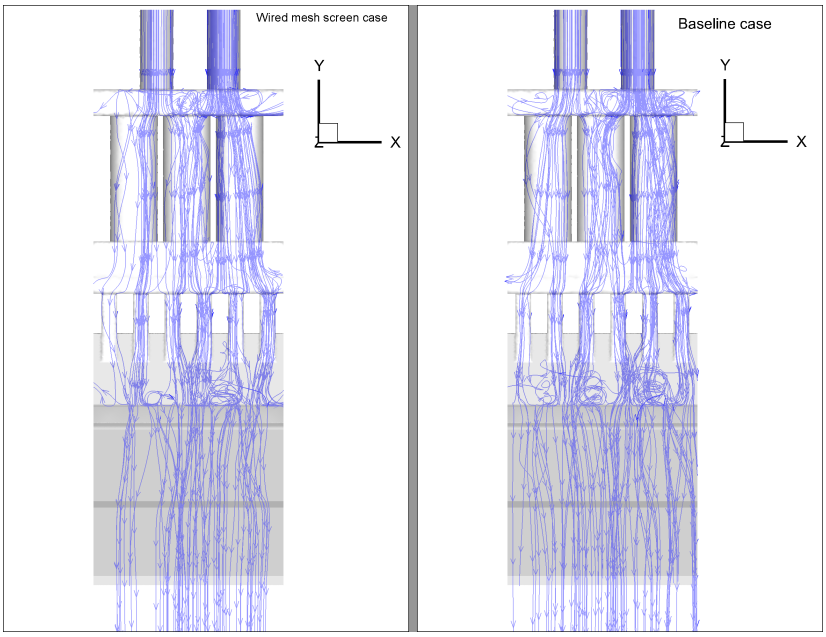

Figure 34 - Pathline plots comparison between wire mesh screen case (left) and baseline case (right)

3.2.2 Pathline and Cross-flow Analysis

Figure 33 shows the magnitude of the X component of the velocity. The wire mesh screen eliminates the upstream flow pattern in the jet region and reduces the x-component velocity. However, the path lines shown in Figure 34 still shows some crossflow within the airplane channel and the jet region, both.

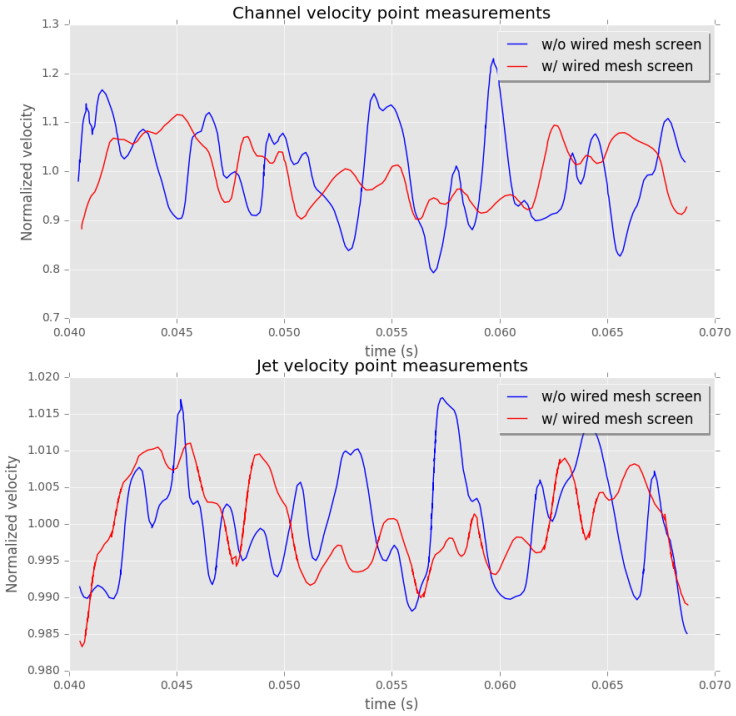

Figure 35 - Velocity time series plot

3.2.3 Time Series data Analysis

The time series data of the point measurements (Figure 24) were analyzed to study the effect of the wire mesh screen on the magnitude of the unsteady fluctuations. Figure 35 shows the velocity time history at a point in the middle of the channel and a corresponding point in the jet. We can see the oscillation magnitudes were suppressed by the wire mesh screen both in the air plate channel and jet region. Figure 36 shows the PSD plot of the middle air plate channel point and jet point. It is seen that the low-frequency component was greatly reduced.

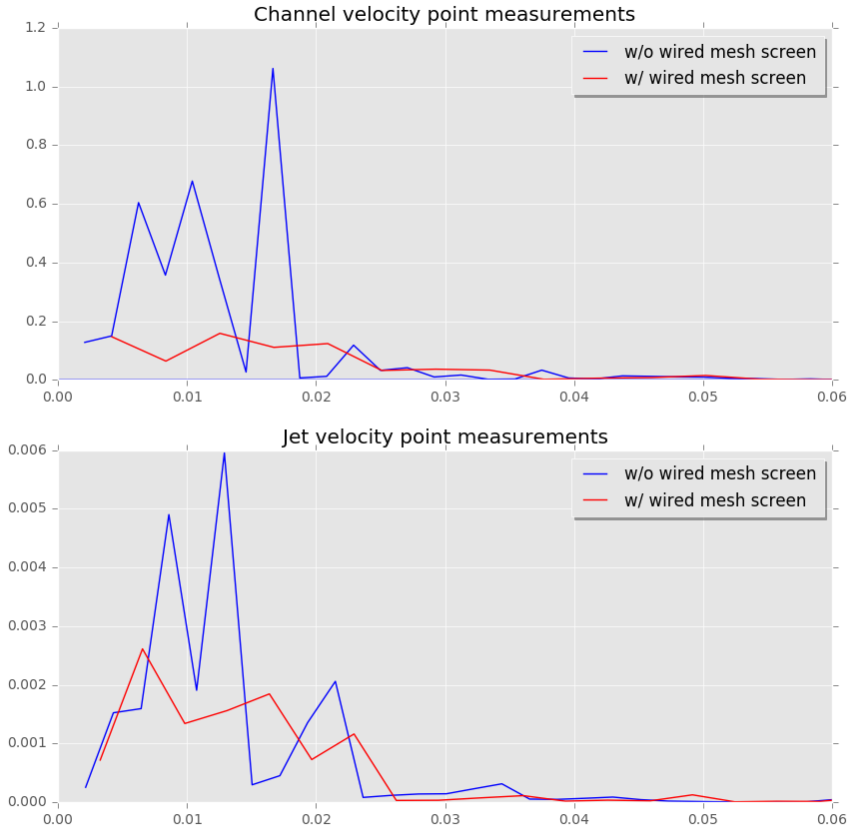

Figure 36 - PSD plots of velocity point measurements

3.3 Effects of Honeycomb

One of the disadvantages of the wire mesh screen is that the crossflow cannot be completely suppressed. As we discussed in Chapter 1, the cross flow in the jet region has a great impact on the quality of the non-woven materials. Honeycomb structures have been widely used in the industry as a flow straightener, and we next examine whether this property can help to eliminate the cross flow and also maintain low turbulence intensity and unsteadiness.

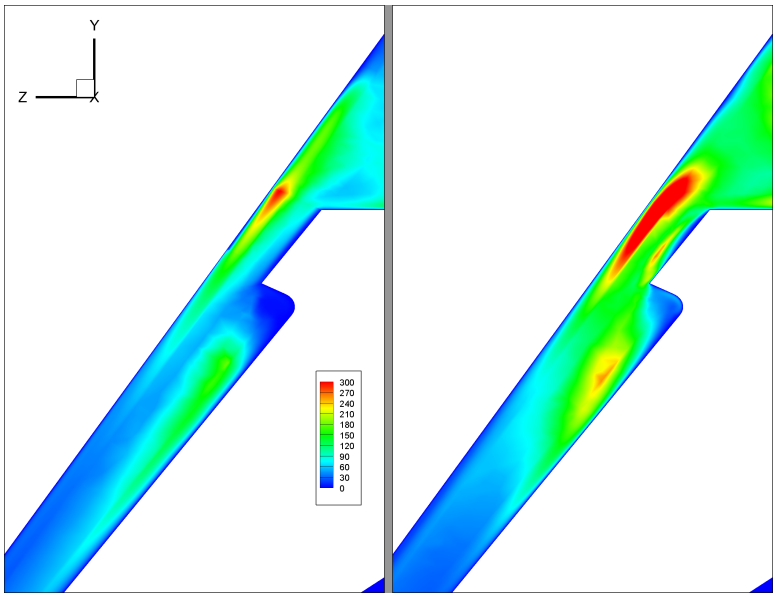

Figure 37 - TKE contour comparison between the honeycomb case (left) and baseline case (right)

3.3.1 Velocity Magnitude and TKE Contour Analysis

The TKE contour and velocity magnitude contours with (left) and without the honeycomb (right) are plotted in Figure 37 and Figure 38. From the velocity vector plot, we can see that the honeycomb straightened the flow directions. The reversed flow region near the lower surface of the air plate channel was eliminated. The separation bubble size also decreases in size, and the vortex near the lower surface becomes smaller according to the blue region in Figure 38. The TKE level in the honeycomb region and its downstream region was also reduced.

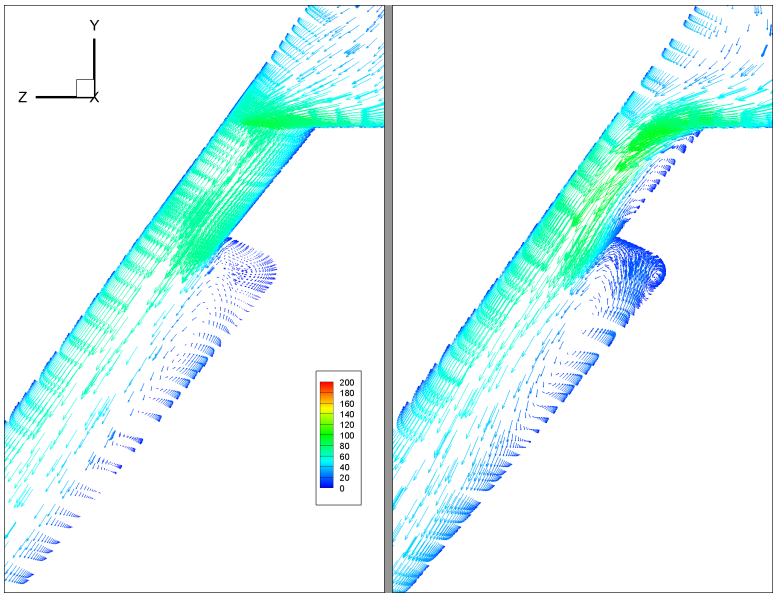

Figure 38 - Velocity vector plot comparison between the honeycomb case (left) and baseline case (right)

A slice was across the air plate channel was chosen to visualize the effects of the honeycomb on the flow field in this region. Figure 39 shows the velocity magnitude on this slice across the air plate channel and Figure 40 shows the TKE contour. With the installation of the honeycomb, the downstream velocity magnitude field is more evenly distributed and the TKE level is lower than the baseline case.

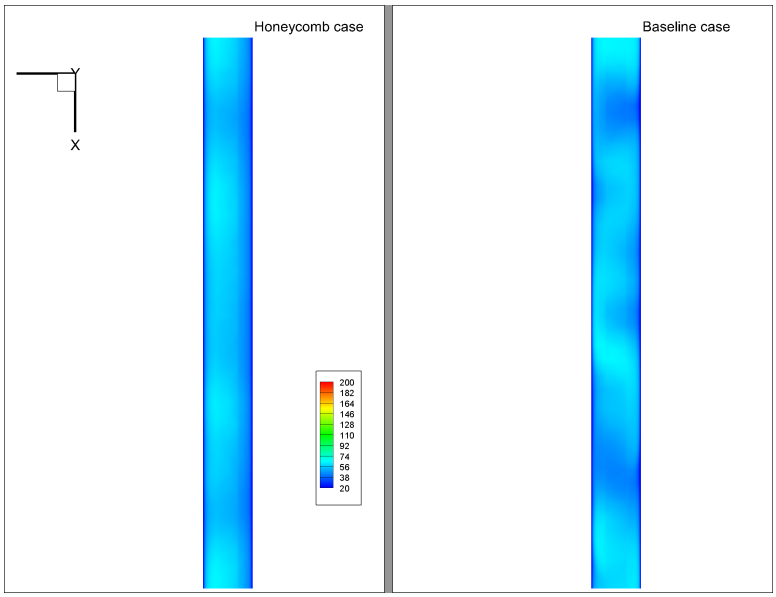

Figure 39 - Velocity Magnitude contours comparison between the honeycomb case (left) and baseline case (right)

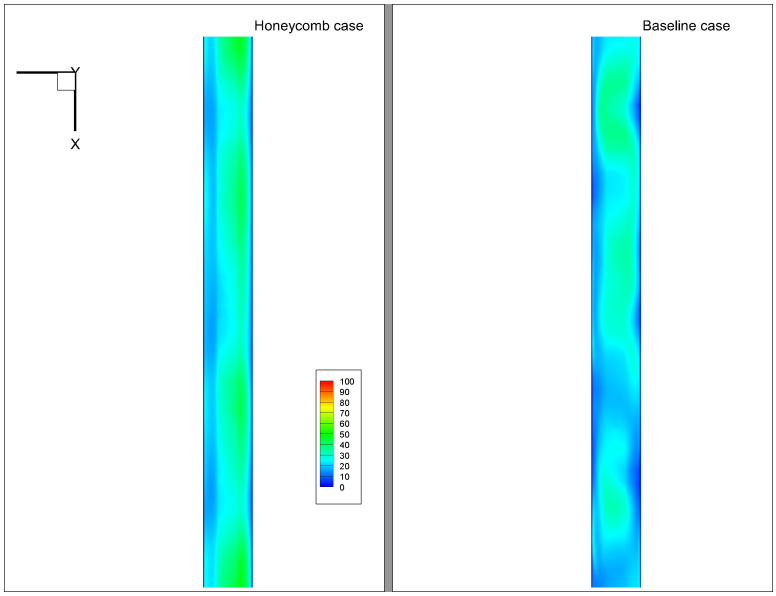

Figure 40 - TKE contours on a slice across the air plate channel with honeycomb case (left) and baseline case (right)

Figure 41 shows the velocity magnitude contours on a Z= Constant plane as discussed previously. The periodic flow pattern, seen as streaks in the air plate channel, is eliminated.

We can observe three high velocity spikes in the jet flow region, and while in the baseline case we observe several irregularly spaced spikes.

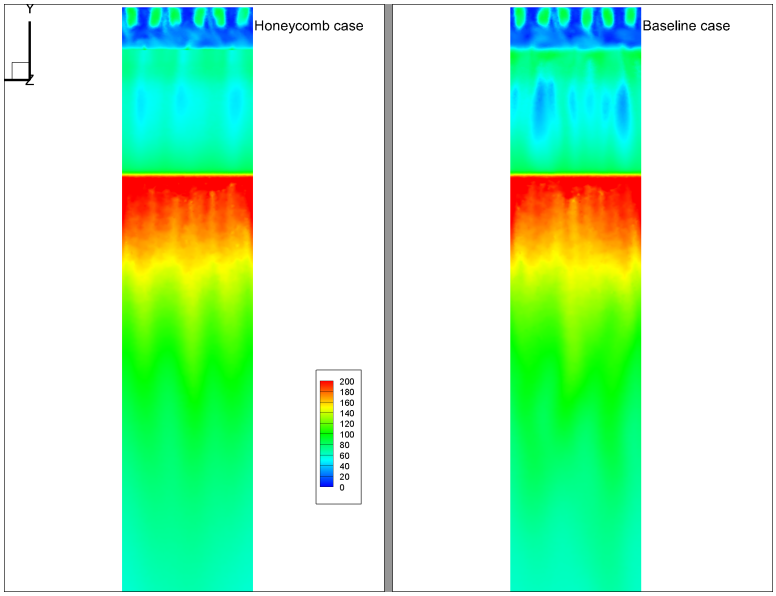

Figure 41 - Velocity Magnitude contours on z = constant slices with (left) and without (right) the honeycomb

Figure 42 illustrates corresponding TKE contours in the baseline case, we can see multiple high-level TKE flow bands in the air plate region, caused by the upstream air channels. In the honeycomb case, those flow structures were eliminated by the honeycomb, and the TKE level remains at a relatively low level. However, in the jet flow region, the TKE level was not reduced to such a low level. The high TKE region in the jet it is not related to the upstream flow TKE level. The reason is the high local production of TKE, caused by the high levels of vorticity in the impingement jet region. Nevertheless, with the honeycomb as a flow straightener, TKE contour in the jet region only has one large spike, while in the baseline case we have three spikes.

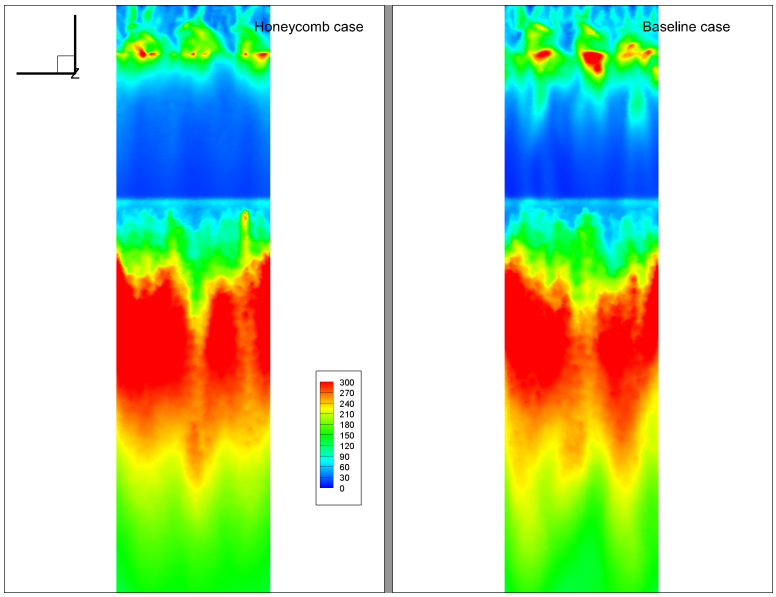

Figure 42 - TKE contours on Z= Constant slices with (left) and without (right) the honeycomb

3.3.2 Pathline and x-component Velocity Analysis

The effects of the honeycomb are further examined with contours of X-component (crossflow) velocity in Figure 43 and path lines in Figure 44. The honeycomb structure greatly reduces the magnitude of the X-component velocity compared to the baseline case. In the air plate channel region, the flow direction was straightened along the flow direction, and the path lines are all parallel to each other as shown in Figure 44. In the jet flow region, the magnitude of the X-component velocity increases due to the increase of the turbulence intensity. However, with the more parallel upstream flow, the magnitude of the cross flow is significantly lower than for the baseline case.

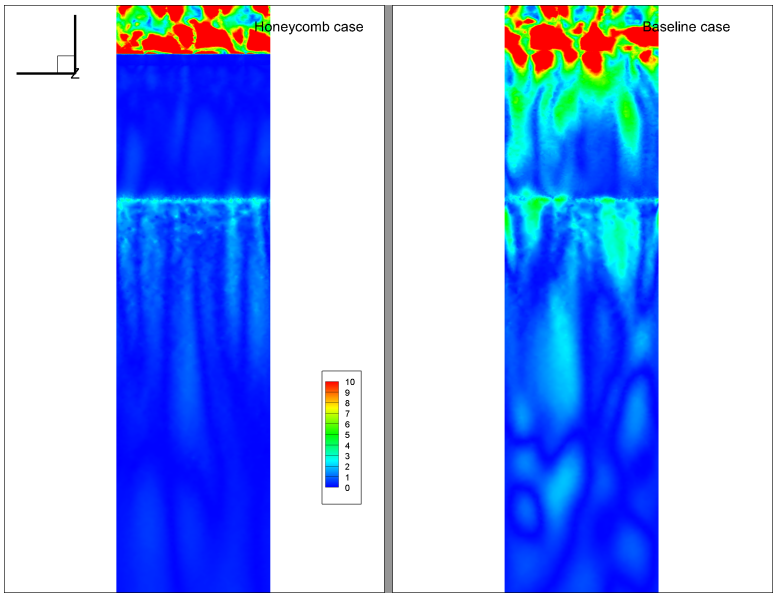

Figure 43 - X-component velocity magnitude contour

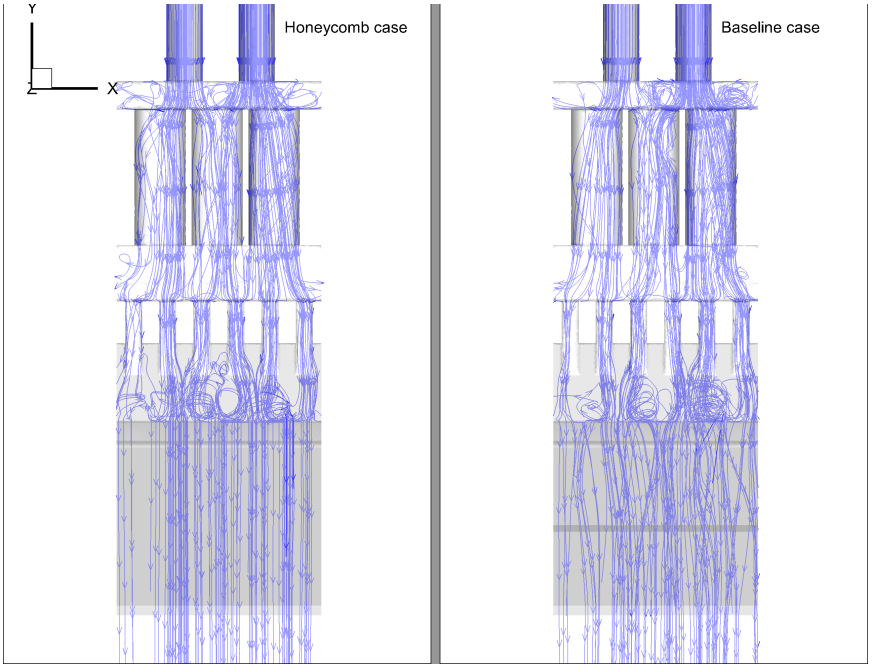

Figure 44 - Pathline of the honeycomb case

3.3.3 Velocity Time Series Analysis

The time history of the velocity magnitude with and without the honeycomb have been examined. Figure 45 shows the normalized velocity time series at two locations, and we can see the magnitude of the velocity fluctuation was greatly reduced with the honeycomb. Figure 46 shows the PSD of the velocity time series, from which we can see that the oscillations have been suppressed by the honeycomb.

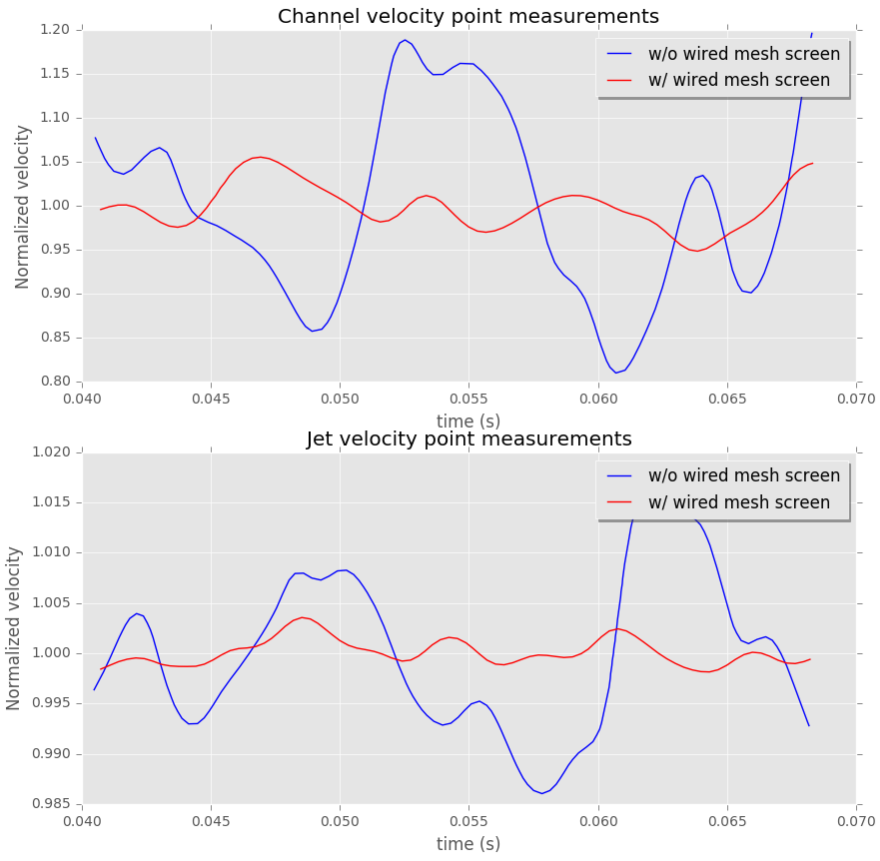

Figure 45 - Velocity time series of the middle point measurements

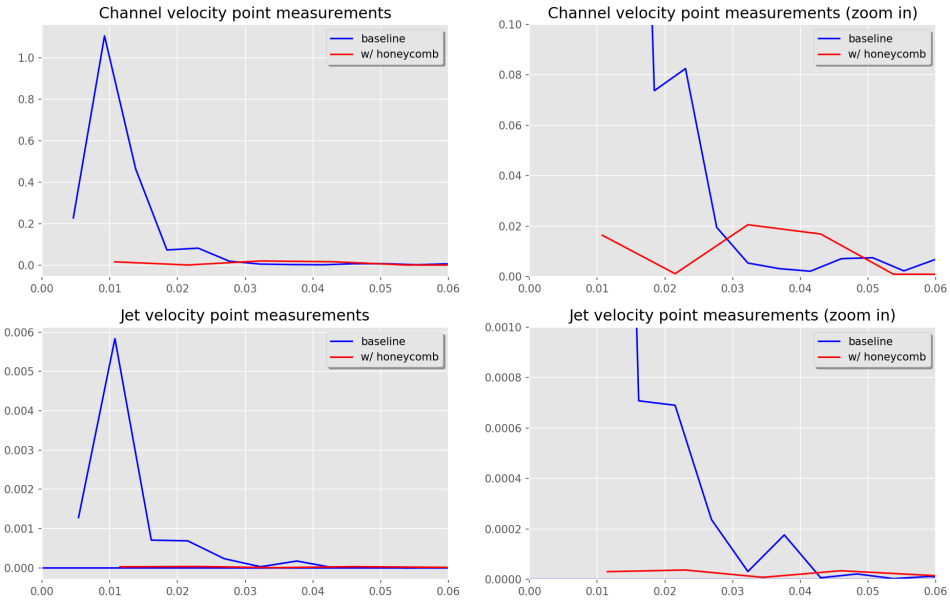

Figure 46 - PSD plots of the velocity times series of honeycomb case

CHAPTER 4. CONCLUSIONS

In this study, the flow field in an industrial Melt-Blowing process system and the corresponding jet flow region was investigated using a CFD study. A CAD model, based on a real-world industry configuration, was used for modeling the computational domain. Two different flow fluctuation reduction devices were studied, a wire mesh screen and a honeycomb - using the porous media condition in ANSYS FLUENT. The parameters for the porous media zone condition were specified based on the curve fits for the pressure jump as a function of the flow rate.

The baseline case without any flow fluctuation reduction device was first studied. It was shown that the flow field is highly unsteady, and that the flow fluctuations were self-excited. The flow fluctuation was caused by the formation and shedding of a separation bubble, and the presence of velocity inflection in the air channel and mixing channels. The oscillations of the velocity magnitude of the channel flow and impinging jet flow was compared, and it was shown that the oscillations of the normalized velocity in the jet region was much smaller than that of the air plate channel. The correlation coefficients of all point measurements were analyzed to show that the upstream flow in the air plate channel has a great impact on the jet flow. Furthermore, power spectral density plots show that the velocity fluctuation was dominated by low-frequency components, which is consistent with the oscillation of the separation bubble in the mixing channel.

Wire mesh screen cases were next studied to investigate the effect of a wire mesh screen on the flow fluctuation and the flow inhomogeneous on the x-direction. The velocity magnitude contour, TKE contour, path lines and time series data were all analyzed and

compared between the baseline case and wire mesh screen case. The PSD plots also show that the low frequency component of the velocity fluctuation was greatly reduced with a small increase in the high frequency component. The results show that the wire mesh screen can greatly reduce the downstream TKE level and inhomogeneity in the x-direction, but some cross flow still exist in the jet regions. The cross flow could impact the quality of the non-woven material, so a honeycomb was used as a flow straightener to overcome this issue.

The honeycomb flow straightener was similarly modeled using a porous media zone with one direction with a much lower resistant coefficient. The flow direction was restricted to the direction parallel to the main flow direction. The path line plot shows that the cross flow was eliminated the jet flow region, although the TKE level in the downstream was higher than that of the wire mesh screen case. The cross-flow field was greatly suppressed.

With the usage of wire mesh screen and honeycomb, it's difficult to completely eliminate the flow fluctuations. However, we do see great reductions in the TKE levels and cross flow velocities in the impinging jet region. The wire mesh screen can reduce the turbulence intensity and make the downstream flow more evenly distributed, although of cross flow exists. The honeycomb could help suppress the cross flow in both air channel and jet flow region, but the turbulence intensity is not reduced to the same level as the wire mesh screen case.

REFERENCES

ANSYS, I. (2009). ANSYS FLUENT 14.0 Theory Guide. Retrieved from http://www.afs.enea.it/project/neptunius/docs/fluent/html/th/main_pre.htm

ARA. (2017). TWT Honeycomb Flow Strightener. Retrieved from http://ara.co.uk/pt/new-redirector-page-pt/image-library/the-facility/

Chen, Z. J., & Przekwas, A. J. (2010). A coupled pressure-based computational method for incompressible/compressible flows. *Journal of Computational Physics*. http://doi.org/10.1016/j.jcp.2010.08.029

Haynes, B. D & Cook, M. C. (2005). US Patent 6,972,104 B2.

Kimberly Clark Coraporation. (2000). Air Flow through Woven Stainless Steel Mesh.

Krutka, H. M., Shambaugh, R. L., & Papavassiliou, D. V. (2002). Analysis of a melt-blowing die: Comparison of CFD and experiments. *Industrial and Engineering Chemistry Research*. http://doi.org/10.1021/ie020366f

Li, C. G., Liu, Y., & Cheung, J. C. K. (2013). Wind Tunnel Test of Honeycomb in Improving Flow Quality. *Advanced Materials Research*, *774–776*, 275–278. http://doi.org/10.4028/www.scientific.net/AMR.774-776.275

Miettinen, A., & siikonen, T. (2015). Application of pressure- and density-based methods for different flow speeds. *International Journal for Numerical Methods in Fluids*.

http://doi.org/10.1002/fld.4051

Obot, N. T., Trabold, T. A., Gandhi, F., & Graska, M. L. (1986). Velocity and Temperature Fields in Turbulent Jets Issuing from Sharp-Edge Inlet Round Nozzles. *Industrial and Engineering Chemistry Fundamentals*. http://doi.org/10.1021/i100023a022

Shambaugh, R. L. (1988). A macroscopic view of the melt-blowing process for producing microfibers. *Industrial & Engineering Chemistry Research*. http://doi.org/10.1021/ie00084a021

Sun, Y. F., Liu, B. W., Wang, X. H., & Zeng, Y. C. (2011). Air-flow field of the melt-blowing slot die via numerical simulation and multiobjective genetic algorithms. In *Journal of Applied Polymer Science*. http://doi.org/10.1002/app.34760

Tennekes, H., & Lumley, J. L. (1972). *A First Course In Turbulence*. *MIT*. http://doi.org/10.1088/1751-8113/44/8/085201

Wang, Y., & Wang, X. (2014). Numerical analysis of new modified melt-blowing dies for dual rectangular jets. *Polymer Engineering and Science*. http://doi.org/10.1002/pen.23536

Zuo, F., Tan, D. H., Wang, Z., Jeung, S., MacOsko, C. W., & Bates, F. S. (2013). Nanofibers from melt blown fiber-in-fiber polymer blends. *ACS Macro Letters*. http://doi.org/10.1021/mz400053n